

6/p.

X69 ~~15539~~  
NASA CR-51064  
N 65-81116

Preliminary Results on Effects of Hypervelocity

Impacts on Space Radiator Tubes

by J. W. Gehring and Seymour Lieblein

A. R. S. Paper No. 2544-62

Paper Presented to the American Rocket Society  
Space Power Systems Conference  
Santa Monica, California, September 25-28, 1962

A.R.S. Paper No. 2544-62

"Preliminary Results on  
Effect of Hypervelocity Impact on Space Radiator Tubes"

by J. W. Gehring\* & S. Lieblein\*\*

ABSTRACT

15539 over

This paper will describe the results of the first phases of an experimental research program aimed at determining the damage that would be inflicted upon space radiator configurations by the impact of a meteoroid. Meteoroid hazards are discussed, and the present knowledge of crater formation under conditions of hypervelocity impact is analyzed. The experimental program was conducted on the ballistics range facilities of the General Motors Corporation Defense Research Laboratories in Santa Barbara, California. Glass projectiles (.016 and .040 g.) were accelerated to hypervelocities of 23,000 to 26,000 fps and impacted against targets typical of radiator materials and configurations under simulated operating conditions. The experiments tested radiator tube configurations in vacuum, treating such variables as tube liner, tube inner diameter, armor thickness and material, operating temperature, and angle of impact.

---

Work described in this paper was carried out under NASA Contract No. NASw-468 under the technical direction of the Flow Processes Branch of the NASA Lewis Research Center. Acknowledgment is made to A. R. McMillan of General Motors Corp. for conducting the impact firings, and to N. Clough and I. J. Loeffler of the NASA Lewis Research Center for assistance in the preparation of the text.

\*J. W. Gehring, Head Hypervelocity Impact Group, GM-Defense Research Laboratories, Santa Barbara, California, Member ARS

\*\*Seymour Lieblein, Chief, Flow Processes Branch, NASA Lewis Research Center, Cleveland, Ohio, Member ARS

~~Available to NASA Offices and  
NASA Centers Only.~~



Significant differences between hypervelocity impact into flat plates and into aluminum and columbium tube configurations were observed. The results indicated that internal surface dimpling and spalling should be important considerations in radiator tube design.

## INTRODUCTION

This paper was presented to introduce to Space Power System Designers an experimental research program aimed at defining the meteoroid hazard to space vehicles. In a companion paper<sup>1</sup> presented by Messrs. Loeffler, Lieblein, and Clough to the ARS Space Power Systems Conference, we were instructed in an analytical approach to the definition and composition of meteoroids, and the application of this knowledge to the assessment of the meteoroid damage problem for waste heat radiators of space power systems.

Their analysis represents a detailed application of the current concepts of the nature of meteoroid behavior and their impact effects. Specific insight into the damage likely to be incurred by a meteoroid collision can be obtained, for example, from Ref. 2-4. Unfortunately, however, there is very little background in the area of the phenomena of hypervelocity meteoroid impact under conditions likely to be experienced by a space radiator. In particular, it is necessary to compare the specific voyage of the vehicle and the predicted meteor hazard against an evaluation of the impact damage in terms of: the radiator material; the radiator construction and configuration; the in-flight operational environment of high material temperatures and low ambient pressures; and the reaction of a pressurized liquid or gas in the tube.

In consideration of these problem areas, an experimental research program was begun under the direction of the NASA-Lewis Research Center to assess the impact damage by a meteoroid against a variety of targets simulating radiator

materials and configurations under operating conditions of elevated temperature and low ambient pressure. The aim of the research program is to obtain data related to the broad concepts of protecting radiators against damage from impacting meteoroids.

The first phase of the program was intended to cursorily explore the nature of hypervelocity impact damage in radiator tube configurations typical of application to space power systems such as SNAP-8. Preliminary results of this first phase have been obtained with aluminum and columbium tube configuration and will be reported herein.

#### DESCRIPTION OF HAZARD

The immediate concern to the designer of a space radiator system is the likelihood of collision with meteoroids of given properties in space, and the resultant damage that these meteoroids could cause to the system. Since it is impossible to control the occurrence of meteoroids in space, the designer must choose protection that is capable of protecting a radiator from impact damage by the largest meteoroid it is expected to encounter for a given statistical probability on its specific flight path and time of exposure. Consequently, the meteoroid hazard to a space vehicle must be considered in terms of frequency of encounter, direction of influx, mass distribution, relative velocity, the physical properties of meteoroids, and the vulnerable area of the radiator and mission time. Because of the large surface areas involved, meteoroids of most vital interest to radiator designers are the particulate matter in the range of mass from  $10^{-2}$  to  $10^{-4}$  grams, large enough and frequent enough to be of some hazard. Also of concern is the finer material capable of etching the high emittance coating of the radiator surface. The techniques used in

the recent publications by Whipple<sup>(5)</sup> and by McCracken & Dubin<sup>(6)</sup>, by which the frequency of occurrence of meteoroids in space have been predicted, include photographic and radar measurements as well as rocket and satellite measurements. From an analysis of these data, it was possible for Loeffler, et al<sup>(1)</sup> to assess the meteoroid hazard to space radiators in terms of the meteoroid properties, the vulnerable area of typical radiator systems, mission time, and the anisotropic meteoroid flux expected for a given vehicle voyage.

Given that the frequency of occurrence of meteoroids can be predicted, it is now necessary to define the impact damage likely to be sustained by a given radiator design. For space power systems involving liquid metal fluids, the radiator may appear as in figure 1. The fluid-carrying tubes will most likely be composed of a thin corrosion-resisting inner liner surrounded by a sleeve of impact-resisting armor. A typical radiator finned-tube segment is shown in figure 2. The finned radiator segment is made of cast aluminum alloy (0.400" thick) with a Haynes Alloy No. 25 tube liner (.020" thick). The crater shown in figure 2 was caused by a 1/8" diameter glass sphere (0.038 gms) impacting at 23,000 fps. The kinetic energy of the impacting pellet is characteristic of meteoroid energies likely to be encountered in space. The crater (0.3" deep) did not perforate the tube; yet, the intense shock induced beneath the crater caused the liner tube to be dimpled, thus causing a constriction of the inner diameter of the tube. This particular shot was fired at room temperature, hence the aluminum armor behaved in a semi-brittle fashion evidenced by the brittle spallation around the periphery of the crater.

A physical description of the mechanism of crater formation in simple plate targets under normal hypervelocity impact is now possible within the

state of the art. Much experimental data are available and empirical relationships have been well established to describe the phenomena. The model that has been evolved from the combined theoretical and experimental studies by many researchers has been illustrated schematically in Ref. 4.

Although there exists no detailed mathematical theory by which to describe the phenomena of normal hypervelocity impact, many relationships have been established and verified experimentally. These relationships will be discussed and their ability to accurately predict resultant crater volumes will be noted. The most important of the phenomena observed in previous studies is that a linear relationship exists between the volume of the crater resulting from hypervelocity impact and the energy of the impacting projectile. The importance of resistance of the target to shear deformation at high-strain rates is seen to be a controlling parameter to the final crater volume. For example, the Brinell Hardness Number was found to provide a surprisingly good criterion for assigning a value to the strength of the target. However, other significant strength parameter correlations may be determined.

Since space radiators may be operating at temperatures from 500°F to 2000°F, the effects of changing target temperature will be seen in an increase in the resultant damage. Results shown in Ref. 4 demonstrate the effects of increased target temperature. Therefore, it will be necessary to test space radiator tubes under simulated operating conditions in order that a proper appraisal may be made of the damage which has been effected.

## EXPERIMENTAL PROGRAM

The overall objectives of the NASA radiator protection program are threefold: first, to define the principal damage mechanisms involved in the hypervelocity impact of particles against radiator tubes; second, to evaluate the relative effectiveness of various protection methods and concepts; and third, to conduct a systematic study of the significant parameters involved so that a large body of realistic design data covering a wide range of applications can be obtained. Wherever possible, the experimental work will deal with realistic tube targets of applicable materials and configurations at temperatures and in environments characteristic of the radiator design operation.

In general, two basic protection concepts or approaches are currently being considered in radiator design<sup>1</sup>. The first, and more popular is the solid armor approach in which a mass of material is used to surround the fluid carrying members. In this case, the design problem is to allow for just enough mass (i.e. thickness) that will prevent a predefined damage to the configuration. In the second approach, called the bumper approach, various displaced shielded configurations are utilized to accomplish the same objective. For purposes of programming, various composite configurations will also be included in this category. The bumper concepts, for effective evaluation, however, must also include consideration of the effects of heat transfer impedance.

In the effort contained in the present program initial work has been directed toward an experimental study of the armor protection approach. The armor approach was undertaken first because it was felt that the large amount of supporting data available from flat plate firings would enhance an early generation of usable design data. An exploratory set of firings into

armored tube configurations was therefore set up to investigate tube damage phenomena (cratering and internal spalling) and define the important variables involved. It was also hoped to obtain a general grasp of real tube effects to aid in the direction and detailing of the subsequent effort. In addition, the targets and conditions prescribed for this first phase were taken characteristic of current radiator system designs such as SNAP-8, so that any significant results obtained could find immediate application.

For armored tubes, the principal variables expected to influence damage are: armor material and thickness, temperature, inner (corrosion resisting) liner material and thickness, angle of impact, and internal fluid (liquid or gas). The first phase of the program was therefore set up to include most of these variables. Tube configurations used were 356-T51 cast aluminum armor on a HS-25 inner liner and solid columbium - 1% zirconium alloy tubes. The specific shots called for in this first phase are outlined in Table I. It was intended to conduct these firings with 3/32" diameter glass projectiles at a nominally constant velocity. Equivalent protection thicknesses for the aluminum and columbium tubes were determined according to the impact relations of Ref. 1.

## EXPERIMENTAL TECHNIQUES

### Range and Monitoring Instrumentation

All of the tests to date were conducted on a ballistics range, which is fully described in GM-DRL Report ER-62-201A<sup>7</sup>. The basic equipment consists of a gun, a 20 foot free-flight range, and an impact chamber. The 0.22" caliber accelerated-reservoir light-gas gun is shown in Fig. 3. With this gun, it was possible to launch cylindrical plastic models to velocities of 32,800 fps, or sabot metal or glass spheres to velocities of 28,000 fps.

The accelerated-reservoir light-gas gun consists of a combustion chamber in which smokeless powder (IMR Series) is used to accelerate a polyethylene pump piston down a 20 foot long, 1 inch I.D. pump tube; and, in so doing, the pistons compress hydrogen as the driver gas to a pressure of nominally 20,000 to 30,000 psi. At this pressure, a break valve opens at the front end of the high pressure coupling, thus releasing the hydrogen gas into the launch tube behind the model. As the model begins its travel in the 4' long launch tube, the pump piston enters the tapered section of the high pressure coupling. The front face of the pump piston is accelerated, thus maintaining a constant base pressure behind the model during launch. The projectile is launched into the flight range and travels 20 feet before impacting the target. Prior to impact, the projectile travels through a surge chamber (in which the model is separated from the sabot) then into the velocity chamber. Here, the position and time of flight of the projectile are recorded at each of three spark shadowgraph stations (the octagonal chamber shown in Fig. 4). When the model interrupts a photo beam, electronic counters are started, and a short duration spark is set off, exposing a film plate. The measurements of time and distance between stations serve to determine the velocity of the projectile along its trajectory and in particular, at the target. The accuracy of the impact velocity determined in this manner is better than 1.0%.

The model flight is terminated in a specially constructed impact chamber (Fig. 4) which has six viewing ports. Two large windows are located in opposite sides of the target area, and four smaller windows are located on the front of the chamber. The full size door acts as the rear wall of the chamber, to allow easy insertion and removal of the targets. The targets are held by a mount sitting on two rails on the floor of the chamber.

This design allows placement of the target at a uniform longitudinal position with respect to the viewing ports. A variety of targets can be accommodated.

Since the investigation of the damage to a radiator target requires that the targets be impacted while under a simulated space environment, it was necessary to conduct the tests with the target at an elevated temperature and while in a simulated space environment of low ambient pressure. A typical target holder with the heater elements is shown in Fig. 5. This target holder permitted the mounting of the radiator segments and heating them to temperatures up to 1500°F. The requirement for low ambient pressures was met by sealing the impact and velocity chambers and pumping down to pressures of less than 1 millimeter of Hg. Air, or any number of desired gas mixtures, can be introduced into the chambers as test medium. In order to prevent oxidation of the heated targets in these tests, helium was used as the test gas. An Alphatron vacuum gage, calibrated for helium gas, provided accurate pressure measurements within the chambers.

Photographic equipment was used to monitor the impact phenomena. A Beckman & Whitley Model 192 framing camera, capable of framing rates as high as 1.4 million frames per second was used to precisely record the incoming projectile velocity, the phenomena of impact flash, and the motion, velocity, and in a rough sense, the quantity of minute particles being ejected from the crater. With this camera, it was also possible to observe, in a plane across the surface of the target, the growth of the crater in time. A typical B & W sequence of a 1/8 inch glass sphere impacting a space radiator segment at 23,000 fps is shown in Fig. 6.



The Ballistics Range is also equipped with four channels of flash radiographic equipment, capable of viewing the impact at any four pre-selected times during the crater formation (Fig. 4). Each X-ray pulse is 0.07 sec. in duration at a peak output of 100 KV at 1400 amperes. Flash X-ray instrumentation is particularly useful to "see" through the ejecta debris from the crater to determine the composition of the debris; i.e., vapor or solid particles. The combination of X-ray and the B & W camera optical record (Fig. 6) provide a detailed pictorial record of the process of crater formation. For the purpose of brevity, a typical flash radiograph is not included here.

#### Target Preparation

The assessment of target damage to the space radiator is complex and requires precise definition. Prior to testing any of the targets, each target was classified according to both material properties (as indicated by the manufacturer's specification) and by examination of the condition of the material. Since the tests were aimed at simulating actual operating conditions, each target was annealed for eight hours at the test temperature prior to firing the shot. In the tests conducted thus far, the annealing and test temperature was 700°F. This pre-firing heat treatment procedure was significant in that the aluminum targets undergo a phase change at 700°F after several hours anneal, resulting in reducing the Brinell Hardness number from a nominal 52 to a value of 20. The BHN is used here as a measure of the strength of the material; hence, the lower the BHN, the more damage is likely to be caused on impact<sup>4</sup>. Following the shot, the targets were cooled to room temperature and the damage assessed.

## EXPERIMENTAL RESULTS

A complete tabulation of the results and identifying parameters for all data shots fired in conjunction with the initial phase of the program is given in table II. Crater depth and dimple height were defined with respect to the original surfaces as shown in Fig. 7.

In addition to measurements of crater depth and diameter, targets were sectioned to show the extent and nature of the damage. To assist in the reporting of the observed damage, a damage evaluation code was established as shown in Fig. 8. The firings reported in table II include most of the specific shots called for in table I and additional exploratory or development shots into the subject targets that supply useful information. The velocities achieved were in the range from 23,000 to 26,000 fps. The projectiles used had a nominal density of 2.7 gm/cc.

The analysis of the experiments will be described under two major headings. The first will include qualitative observations and comparisons. Quantitative assessment of crater depth and onset of spall will be made in a succeeding section.

### Qualitative Observations

Mass scaling. - First, meteoroid mass scaling effects are considered by comparing the damage caused by impact of two projectiles, one a 3/32" glass sphere, the second a 1/8" glass sphere, each impacting an aluminum-armored HS-25 tube at a nominal velocity of 23,250 ft/sec. (Fig. 9). The targets were at an average environmental operating temperature of 715°F. These projectiles, weighing 0.016 and 0.040 grams respectively, fall into the meteoroid mass-frequency distribution area of interest for radiators (Ref. 1).

In Fig. 9 the 3/32" glass sphere did not perforate the armor, but did cause a dimpling of the inner liner. The 1/8" glass sphere, on the other hand, produced a larger crater diameter and complete perforation of the aluminum armor and the HS-25 liner. Hence, under these conditions of target temperature and projectile density, the "ballistic limit" of this configuration can be defined as being between a meteoroid kinetic energy of  $3.42 \times 10^{10}$  to  $8.5 \times 10^{10}$  ft-lbs.

Target temperature. - Although it was shown in Ref. 4 that by increasing the target temperature one could achieve greater damage to a simple metal plate target, it was not known how the increased temperature would affect a composite target such as those selected for these tests. In one test, a 1/8" glass sphere was fired at an average velocity of 23,300 ft/sec. into each of two targets, one at room temperature, the other at 700°F (Fig. 10). In both cases the radiator complex was perforated. However, in the case of the target at 700°F, the crater area was greater than for the target at room temperature. In addition, the target at room temperature exhibited evidence of brittle spalling around the periphery of the crater indicative of the greater hardness (reflected by the Brinell hardness number) for lower ductility of the material.

Aluminum targets impacted by a 3/32" glass sphere at 400°F temperature and at 700°F are shown in Fig. 11. The increase in temperature resulted in an increase in both crater depth and diameter (crater volume), but did not affect the height of the dimple in the liner. Sections of these targets taken at the center of the crater are shown on the right of Fig. 11. Again, the more ductile nature of the crater at the higher temperature is observed.

Impact angle. - The next variable known to seriously affect the damage sustained by a target under hypervelocity impact is that of the attacking angle of the projectile to the target. In Fig. 12 is seen the results of a

3/32" glass sphere impacting aluminum armor targets at 27° and 70° from the normal at 24,900 fps at room temperature (the photographs were taken normal to the resultant crater). Oblique impacts at two angles for aluminum armor targets at 700°F are shown in Fig. 13. Several important results should be pointed out. First, all of the craters appear hemispherical, thus assuring that the impacts were typical of the hypervelocity impact regime. Secondly, the depths of penetration and the resulting crater volumes decrease as the impact angle increases. According to previous investigations with plate targets (Refs. 4 & 8), these effects can be accounted for empirically by measuring the energy of the attacking projectile in terms of its normal component of velocity. Hence, as the angle of obliquity is increased, the energy of the projectile and corresponding depth of penetration should diminish with the cosine of the angle of impact.

The phenomena of reduced penetration with angle of obliquity was also observed for the columbium tube targets (Fig. 14). The results of Fig. 14 add further verification to the observation that as long as the normal velocity of the projectile does not fall below that required for hypervelocity cratering, the resultant crater will be a hemisphere although much reduced in volume.

Internal damage. - It was indicated earlier that radiator tube design should also be concerned with the possibility of internal damage effects such as spalling and dimpling even in the absence of a penetration of the tube wall. The existence of such effects in columbium and aluminum tubes were indeed verified as indicated in Fig. 15. The deleterious effects resulting from the injection of spalled fragments or the constriction of the fluid flow cannot be disregarded. It is not sufficient, therefore, to merely observe the crater and measure depth of penetration in assessing target

impact damage for application to radiator tube configurations.

Inner liner. - The beneficial effects of having an inner liner can be seen in Fig. 16. One target was lined with a .020 inch thick Haynes 25 liner, the second target had no liner, but the aluminum armor was made thicker, thus keeping the weight constant. The inner HS-25 liner, although dimpled on the inside, prevented spalling of metal into the tube. Even when the projectile size was increased to a 1/8 inch sphere, spalling was still prevented by the liner, although the dimpling was more severe, as shown on the right in Fig. 15. A tough inner liner is therefore of utmost importance in preventing spall particles from being ejected into the coolant-carrying fluid.

A typical impact crater section of an aluminum target with an HS-25 liner is shown in Fig. 17. Here, the spalling of the armor material beneath the crater itself can be clearly seen, in addition to the dimpled HS-25 liner and the delaminating that has occurred between the liner and the armor. The manner in which the steel liner restricts the flaking and breaking away of the spalled particles is clearly depicted. Of a much more subtle nature, is the delaminating that has occurred at a distance far removed from the dimpled section itself. A close-up view of points A and B in Fig. 17 can be seen in Fig. 18. Here at a magnification of 120X and 300X, respectively, the crater section at points A and B can be seen in detail. At point A severe delaminating has occurred due to the fact that the steel liner was pulled away from the armor, and the bonding material failed. Section B shows another interesting observation. Here, it is believed that some delaminating is not associated with the formation of the crater, but rather, a failure of the bond during fabrication of the radiator section. The different coefficients of expansion of aluminum and HS-25 no doubt resulted in a

poor bond, since this effect was observed in all of the target sections prior to conducting the impact experiments. Delamination can affect radiator performance by reducing section strength and heat transfer properties.

Tube effect. - In applications of cratering data to radiator tube design, it has been assumed that the depth of penetration in flat plate targets is representative of the penetration into tube walls of identical thickness. This was not found to be the case, and a significant effect of tube radius on impact damage was observed. Figure 19 shows impact into a columbium flat plate (radius =  $\infty$ ) and into a 0.46 I.D. columbium tube of the same wall thickness under identical test conditions. Complete suppression of spallation was found in the case of the tube, although the depths of penetration were essentially the same. A similar result was obtained for an unlined aluminum tube as shown in Fig. 20. The results show the tubular section not perforated, yet the flat plate was completely perforated. A more dramatic example of the tube radius effect with the cast aluminum is shown in Fig. 21. The section photographs show the results of impact into tubes of widely different inside diameters, (2.5 and .125 in.) under identical impact conditions and equal wall thicknesses.

The ability of the tubular target shape to sustain the impact damage is believed to stem from the fact that the shock propagation through the circular section is affected by more free surface. Consequently, the rarefaction waves which act to diminish the intensity of the transient pressure pulse react more quickly, thus weakening the shock, and consequently diminishing its ability to cause spall on the under surface. If this observed tube radius effect is verified by further data, it would indicate considerable advantage in using small diameter tubes. Small inner diameter results in less required

protection thickness, smaller vulnerable area (tube outer diameter) and lower tube weight for a given thickness.

Protection criterion. - The final qualitative comparison to be drawn from the experiments conducted is the effect of damage protection criterion. Figure 22 shows an impacted columbium tube and a tube of aluminum armor and HS-25 liner designed for approximately equal weight of protective thickness. The poorer performance of the columbium alloy on this basis is indicated. Figure 23 shows the results of impact into columbium and lined aluminum tubes designed for equal protection according to the relationships of Ref. 1. In both cases, no perforation was observed.

#### Quantitative Analysis

The previous section of the paper has presented a discussion of some of the principal qualitative observations obtained from the results of the initial firings. In addition to exploring and defining the phenomenological aspects of impact into radiator tube configurations, the program also has as its ultimate objective the generation of accurate analytical relations for use in design. Although the initial phase of the program was not specifically designed as a systematic parametric study, it was possible to obtain some preliminary quantitative information from the firings.

It was pointed out early in the paper that a detailed mathematical formulation by which to accurately predict the damage by a meteoroid to space radiator configurations does not exist. The theoretical approaches of Bjork, Riney, Chou and others<sup>9</sup> have made significant advances in the analytical approach; however, the treatments do not account in detail for the effects of increased target temperature, effect of variations in target and projectile material, impacts at angles of obliquity, and the spalling,

dimpling, or delaminating of thin and composite targets. A number of empirical relationships have been offered in the literature (Refs. 1, 4, 9 & 10) which do permit at least an approximation of the depth of penetration which might occur under limited conditions. These relationships for normal impact are of the form (Ref. 4)

$$\begin{aligned} P/d_p &= \left[ \frac{12 \times 10^{-9}}{2\pi} \left( \frac{E}{B_t} \right) \right]^{1/3} / d_p \\ &= K/d_p \left( \frac{E}{B} \right)^{1/3}, \quad K = 1.24 \times 10^{-3} \quad \text{cgs units} \end{aligned} \quad (1)$$

or from (Refs. 1 & 10)

$$P/d_p = \gamma \left( \frac{\rho_p}{\rho_t} \right)^\phi \left( \frac{v}{C_t} \right)^{2/3} \quad (2)$$

For oblique impact, the normal component of velocity is used in both the above equations, that is,  $P \propto (\cos \lambda)^{2/3}$ . These relations, however, were obtained from impact into thick flat plate targets, and it is not known to what extent they will be valid for tubular targets.

Some preliminary correlations pertaining to several factors involved in the above relations for depth of penetration have been established from the initial limited firings. These relate to the effects of target temperature, angle of impact, target material, surface curvature (tube diameter), and liner thickness. In these plots, the values of depth of penetration used are the values corrected to a common velocity of 25,000 ft/sec according to the  $2/3$  power of the velocity (designated by  $P^*$ ). In addition, only penetration values for  $P/t_a$  less than .75 were included in order to eliminate "thin-target" effects. Each data point is identified by its corresponding target number.

Angle of impact. - The available data on variation of depth of penetration with angle of impact are shown in Fig. 24 for cast aluminum tubes at two temperatures. The best-fit variations for the  $(\cos \lambda)^{2/3}$  relation are also shown in the figure. On the basis of these analytical relations, it was



possible to normalize the data with respect to  $P^*$  at  $\lambda = 0$  as shown in Fig.

25. It is thus seen that the data is very well represented by the  $(\cos \lambda)^{2/3}$  relation, indicating the significance of the normal component of velocity in determining penetration depth for the aluminum tubes.

Target temperature. - The available information on variation of depth of penetration with temperature for normal impact for identical conditions is shown for cast aluminum targets in Fig. 26. The value of  $P^*$  for normal impact was obtained by correcting for angle of impact according to the  $(\cos \lambda)^{2/3}$  relation as substantiated in Fig. 25. According to Eq. (1) depth of penetration should vary as  $(1/B)^{1/3}$ , and according to Eq. (2) the variation should follow  $(1/Y_t)^{1/3}$ . The best fit of the experimental data for the functional variations based on modulus of elasticity and Brinell hardness number are shown on the figure. The data variation is seen to be reasonably described by both analytical relations.

Surface curvature. - The existence of a surface curvature or tube radius effect on depth of penetration is strongly indicated in Fig. 27, which plots depth of penetration for normal impact against ratio of tube wall thickness to outer radius for aluminum and columbium tubes at 700°F. The lower limiting value of  $t_a/R_o = 0$  corresponds to a flat plate (zero curvature), while  $t_a/R_o = 1$  represents the upper limit of a solid cylinder (maximum curvature for a given thickness). It should be noted that the region of fall off in penetration depth at high values of  $t_a/R_o$  corresponds to practical values of tube inner diameter (.50 in. and less). However, although no inner surface damage was observed for these high  $t_a/R_o$  points, it is not known whether a quantitatively comparable decrease in required thickness will be observed for the avoidance of incipient spalling or dimpling. However, it is clear

from the photographs of Figs. 19, 20, and 21 that a substantial decrease in spalling and dimpling can be expected for reduced tube size.

The extension of the faired curves through the data points to  $t_a/R_o = 0$  permits the normalizing of the data with respect to flat-plate penetration ( $P^*$  at  $t_a/R_o = 0$ ) as shown in Fig. 28. The aluminum and columbium tubes are seen to fall on essentially the same curve, indicating a possible uniform effect for both materials. However, the establishment of a general empirical correction relation for tube curvature based on these limited data is considered premature.

Although a good preliminary correlation has been obtained on the basis of the ratio of wall thickness to outer radius, this may not necessarily be the most significant physical parameter. It can be reasoned that the size of the impacting projectile particle might be significant, and a ratio of particle diameter to outer radius might also be involved.

Tube liner thickness. - The effects of variation of tube liner thickness on depth of penetration and inner surface dimple height is shown in Fig. 29 for aluminum armor - HS-25 liner combinations of constant total weight (armor thickness decreases with increasing liner thickness). Depth of penetration is seen to increase with increasing liner thickness. The reason for this is not clear. Since the thick liner shots represent values of  $P/t_a$  greater than .75, the increased penetration may be a "thin target" effect, or the effect may be due to the interaction of the liner on the shock variations in the armor. It is also observed that depths of penetration greater than the armor thickness can be obtained due to the dimpling of the liner.

Dimpling of the liner is seen to increase as liner thickness decreases, and for some small value of liner thicknesses, the dimple bursts and spalling occurs (the unlined tube showed considerable spalling). As long as the liner

is sufficiently thick to prevent rupture, it appears that there is a sizable variation in liner thickness that can be used at fixed total weight without risk of puncture, at least for the limits covered in the tests.

Materials constant. - The estimation of depth of penetration using the form of Eq. (2) involves a materials constant  $\gamma$  which has been reported to vary from around 1.5 to 2.5 (Ref. 11). In Ref. 1,  $\gamma$  is taken as 2.0, and in Ref. 10,  $\gamma$  is 2.28. The data obtained in the initial phase of the program can also be utilized to obtain an indication of the applicability of these constants. From equation (2), for a tube, we can write

$$\gamma = \frac{P/d_p}{\left(\frac{v \cos \lambda}{C_t}\right)^{2/3} \left(\frac{\rho_p}{\rho_t}\right) \Phi\left(\frac{P_t}{P_\infty}\right)}$$

where  $P/d_p$  is based on the measured depth of penetration in the tube target,  $\rho_p/\rho_\infty$  is the correction for tube surface curvature established in Fig. 28, and the other values in the denominator are computed from material properties and test conditions (for Ref. 1,  $\emptyset = 1/2$ ; for Ref. 12,  $\emptyset = 2/3$ ).

Values of  $\gamma$  were computed for the applicable data points as indicated in table III for aluminum and columbium targets. For the 16 cast aluminum targets, the average value of  $\gamma$  was 2.27, in close agreement with the constant of Reference 10. For the columbium targets, however, the calculated average values were substantially lower than the equation values for both references. For the equation of Reference 1, ( $\emptyset = 1/2$ ) calculated  $\gamma = 1.49$ ; while for the equation of Reference 13 ( $\emptyset = 2/3$ ),  $\gamma = 1.79$ .

Similarly, the constant K in equation (1) was calculated for the aluminum and columbium targets as indicated in table III. For the 16 cast aluminum targets, the average value of K was  $1.30 \times 10^{-3}$ , which is slightly higher than the constant proposed. For the columbium targets, as before, the average value of  $K = 1.03 \times 10^{-3}$ , was substantially lower than the proposed constant.

The differences between the values for the cast aluminum and the columbium alloy targets suggests that the  $\gamma$  and K constants cannot be taken as a single value for a variety of target materials. However, in view of the relatively few data points, 4, for the columbium targets, and the fact that these targets were heated in air for 8 hours at 700°F prior to impact and therefore became oxidized, further firings into columbium will be necessary to firmly establish the existence of the differences in  $\gamma$  and K.

The foregoing results, if substantiated, indicate a relatively smaller depth of penetration in columbium than previously estimated. For example, difference in depth of penetration in aluminum and columbium calculated according to Reference 1 may now be 35% smaller. However, this doesn't necessarily mean at this point that the armor thickness (and consequently weight) required to avoid critical damage (spalling or dimpling) will likewise be less. Further tests will be required to establish whether such is indeed the case.

#### SUMMARY OF RESULTS

An exploratory experimental investigation of hypervelocity impact by glass spheres at approximately 25,000 fps into columbium alloy radiator tube targets and cast aluminum targets with and without Haynes 25-inner liners was conducted to explore effects of target temperature, angle of impact, liner thickness, tube diameter, and target material. The major tentative findings of the investigation based on the preliminary data are:

1. Hypervelocity impact can create spalling and dimpling of the tube inner surface in thicknesses substantially greater than the depth of the crater on the outer surface. Spalling and dimpling should therefore be important considerations in tube armor design.

2. Significant differences between impact into tubes and plates were observed. In general, decreasing tube size (increased surface curvature) below an I.D. of around a half inch tended to reduce spalling and depth of penetration. An advantage is indicated in using small diameter tubes.

3. The presence of a thin Haynes-25 liner on the inside of the cast aluminum armor tended to suppress spalling and permit a greater depth of penetration without puncture. However, considerable dimpling can occur.

4. Variation of depth of penetration with impact angle appeared to correlate well with the normal component of the projectile velocity.

5. Increasing depth of penetration with increasing target temperature up to 700°F appeared to correlate well with the variation of velocity of sound (modulus of elasticity) and Brinell Hardness number in the target.

6. After using corrections for real tube effects, the depth of penetration in aluminum was in essential agreement with the predictions of several commonly used empirical relations. However, the depth of penetration in columbium was substantially lower than predicted.

APPENDIX - SYMBOLS

$B_t$  = Brinell Hardness No. of target

$C_t$  = Velocity of sound in target

$d_p$  = Diameter of projectile

$E$  = kinetic energy of projectile, ergs.

$h$  = Dimple height

$P$  = depth of penetration in tube target

$P_\infty$  = depth of penetration in thick target

$P^*$  = depth of penetration in tube target corrected to 25,000 ft/sec.

$t_a$  = armor thickness

$t_l$  = liner thickness

$V$  = projectile velocity

$Y_t$  = target modulus of elasticity

$\gamma$  = materials constant in penetration equation

$\emptyset$  = exponent for density ratio in penetration equation

$\lambda$  = angle of impact (measured from the normal)

$\rho_p$  = projectile density

$\rho_t$  = target density

$K$  = materials constant in Equation (2), cm ergs<sup>-1/3</sup>

## REFERENCES

1. Loeffler, I. J., Lieblein, Seymour, and Clough, N., "Meteoroid Protection for Space Radiators" paper presented at the ARS Space Power Systems Conference, Santa Monica, California, September 1962, ARS Paper No. 2543-62.
2. Bjork, R. L., "Meteoroids vs. Space Vehicles", ARS Journal, June 1961, pp. 803-807.
3. Jaffe, L. D., and Rittenhouse, J. B., "Behavior of Materials in Space Environments", ARS Journal, March 1962, pp. 320-346.
4. Eichelberger, R. J., and Gehring, J. W., "Effects of Meteoroid Impacts on Space Vehicles", ARS Journal, October 1962, pp. 1583-1591.
5. Whipple, F. L., "Dust and Meteorites", Astronautics, August 1962, pp. 40-42.
6. Dubin, M., and McCracken, C. W., "Measurements of Distribution of Interplanetary Dust", The Astronomical Journal, Vol. 67, No. 5, June 1962.
7. General Motors Defense Research Laboratories, "Research Facilities of the Aerospace Operations Department", ER 62-201A, GM-DRL, Santa Barbara, California
8. Bryan, G. M., "Oblique Impact of High Velocity Steel Pellets on Lead Targets", Proceedings of the Fifth Symposium on Hypervelocity Impact, Vol. 1, Part 2, April 1962, pp. 511-534.
9. For additional papers on hypervelocity impact phenomena see: Proceedings of the Third Symposium on Hypervelocity Impact, Armor Research Foundation, October 1958, the Fourth Symposium on Hypervelocity Impact held at Eglin Air Force Base, Florida, April, 1960, and the Fifth Symposium on Hypervelocity Impact held at the Colorado School of Mines, Denver,

Colorado, October, 1961.

10. Charters, A., and Summers, J. L., "High Speed Impact of Metal Projectiles in Targets of Various Materials", Proceedings of the Third Hypervelocity Impact Symposium, Armor Research Foundation, Chicago, Illinois, October, 1958.
11. Rodreguez, D., "Meteoroid Shielding for Space Vehicles", Aerospace Engineering, 19 (12): 20-13, 53-56, December 1960.



## List of Figures

- Fig. 1 - Fin-and-Tube radiator
- Fig. 2 - Impact Crater in Typical Radiator Section, Finned Al Armor over HS-25 tube
- Fig. 3 - 0.22 cal. accelerated-reservoir light-gas gun
- Fig. 4 - Velocity and Impact Chambers
- Fig. 5 - Target Holder with Heater Elements
- Fig. 6 - B & W Sequence of a 1/8" Glass Sphere Impacting a Space Radiator Segment at 23,000 fps.
- Fig. 7 - Notation for Target Damage Measurements
- Fig. 8 - Damage Evaluation Code for Sectioned Targets
- Fig. 9 - Projectile Size Effects, Aluminum With HS-25 Liner Targets  
Armor Thickness 0.400", Liner Thickness 0.020"
- Fig. 10 - Target Temperature Effects, R.T. and 700°F. .400" Aluminum  
Armor with .020" Liner Targets. 1/8" Glass Projectile @ 23,300 fps.
- Fig. 11 - Target Temperature Effects, 400 and 700°F. .400" Aluminum  
Armor with .020" Liner Targets. 3/32" Glass Projectile @ 24,600 fps.
- Fig. 12 - Impact Angle Effects, .500 I.D. Aluminum, .400" Thick, HS-25 Liner
- Fig. 13 - Impact Angle Effects, .500" I.D. Aluminum .400" Thick, HS-25 Liner
- Fig. 14 - Impact Angle Effects, .400" I.D. Columbium .200" Thick, No Liner
- Fig. 15 - Internal Tube Damage
- Fig. 16 - Liner Effects, Aluminum Targets
- Fig. 17 - Typical Impact Crater Section, Aluminum With HS-25 Liner Target
- Fig. 18 - Armor-Liner Interface Photomicrographs Reference Fig. 15
- Fig. 19 - Target Radius Effects, Cb Targets
- Fig. 20 - Target Radius Effects, Al Targets

Fig. 21 - Tube Radius Effects. Aluminum Armor, .446" Thick No Liner

Fig. 22 - Comparison of Equal Unit Weight Aluminum and Columbium Targets

Fig. 23 - Comparison of Equal Protection Schemes (NASA Ref. 1) I. D. Constant

Fig. 24 - Variation of Penetration Depth With Impact Angle. Cast Aluminum Tubes. 3/32" Glass Particle 25,000 fps.

Fig. 25 - Normalized Variation of Depth of Penetration With Impact Angle, Cast Aluminum Tubes, 3/32" Glass Projectile 25,000 fps.

Fig. 26 - Variation of Depth of Penetration with Target Temperature. Cast Aluminum Tubes, Normal Impact. 3/32" Diameter Glass Projectile, 25,000 fps.

Fig. 27 - Variation of Depth of Penetration With Tube Radius. 700°F 3/32" Diameter Glass Projectile, 25,000 fps

Fig. 28 - Variation of Normalized Depth of Penetration With Tube Radius 700°F. 3/32" Glass Projectile, 25,000 fps.

Fig. 29 - Variation of Depth of Penetration & Dimple Height With Liner Thickness. Cast Aluminum on HS-25 Equal Weight Configurations. 3/32" Diameter Projectile, 25,000 fps, 700°F.

#### TABLES

Table I - Phase I Firing Schedule

Table II - Phase I, Data

Table III - Comparison of Materials Constant for Aluminum and Columbium

TABLE 1 PHASE I FIRING SCHEDULE

[Al = 356-T51 cast aluminum. Cb = columbium, 1% zirconium.]

Test variables	Test conditions	Target
Temperature	R.T., 400, 600, 700, 750° F	} Al armor cast on HS-25 liner
Impact angle- tube axis displaced	0, 30, 60, 75-80 deg R.T. and 700° F	
Liner thick- ness, in.	0, 0.020, 0.035, 0.044 at 700° F	
Tube diameter, in.	0.125, 0.46, <sup>a</sup> 1.0, <sup>a</sup> 2.5, ∞ at 700° F	0.446-in.-thick Al 0.320-in.-thick Cb
Material prop- erties	Al vs equiv. mass of Cb Al vs equiv. prot. of Cb 0.125 and 0.460 tube I.D. at 700° F	0.446-in.-thick Al 0.202-in.-thick Cb 0.320-in.-thick Cb

<sup>a</sup>Al only.

TABLE 3 COMPARISON OF MATERIALS CONSTANT FOR ALUMINUM AND COLUMBIUM TARGETS

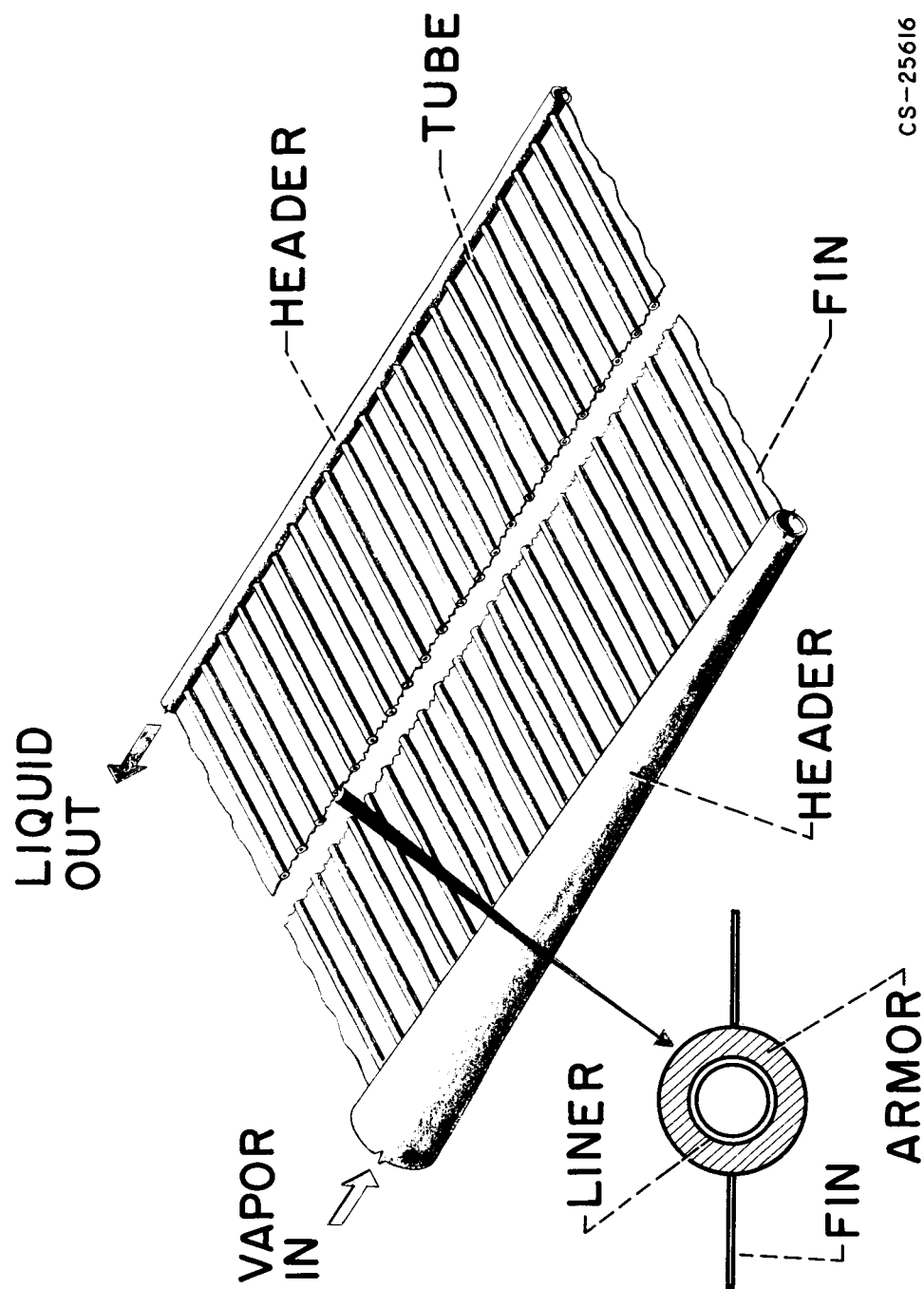
## A. Aluminum (356-T51)

Target no.	Exp. $P/d_p$	Calculated $\left(\frac{V \cos \lambda}{C_t}\right)^{2/3} \left(\frac{\rho_p}{\rho_t}\right)^\varphi \left(\frac{P_t}{P_\infty}\right)$	Calculated $\gamma$	Calculated $(E/B \cos^2 \lambda)^{1/3}$	Calculated K
1	3.19	1.36	2.34	...	...
3	1.79	0.764	2.35	$0.341 \times 10^3$	$1.24 \times 10^{-3}$
5	3.26	1.425	2.29	$0.589 \times 10^3$	$1.37 \times 10^{-3}$
7	1.35	0.762	1.78	$0.326 \times 10^3$	$1.00 \times 10^{-3}$
9	3.36	1.447	2.32	$0.634 \times 10^3$	$1.25 \times 10^{-3}$
27	3.00	1.16	2.59	$0.450 \times 10^3$	$1.57 \times 10^{-3}$
38	3.09	1.39	2.22	$0.585 \times 10^3$	$1.24 \times 10^{-3}$
53	1.68	0.624	2.70	$0.256 \times 10^3$	$1.57 \times 10^{-3}$
54	2.69	1.19	2.26	$0.494 \times 10^3$	$1.29 \times 10^{-3}$
66	3.35	1.35	2.47	$0.620 \times 10^3$	$1.31 \times 10^{-3}$
69	3.26	1.34	2.44	...	...
71	3.90	1.64	2.32	$0.641 \times 10^3$	$1.28 \times 10^{-3}$
79	3.08	1.39	2.22	$0.646 \times 10^3$	$1.14 \times 10^{-3}$
83	3.26	1.80	1.83	$0.584 \times 10^3$	$1.42 \times 10^{-3}$
84	2.57	1.28	2.01	$0.490 \times 10^3$	$1.25 \times 10^{-3}$
85	2.70	1.28	<u>2.12</u>	$0.517 \times 10^3$	<u><math>1.25 \times 10^{-3}</math></u>
		Av.	2.27		$1.30 \times 10^{-3}$

## B. Columbium - 1% Zr

Target no.	Exp. $P/d_p$	Calculated $\left(\frac{V \cos \lambda}{C_t}\right)^{2/3} \left(\frac{\rho_p}{\rho_t}\right)^\varphi \left(\frac{P_t}{P_\infty}\right)$		Calculated $\gamma$		Calculated $(E/B \cos^2 \lambda)^{2/3}$	Calculated K
		$\varphi = 1/2$	$\varphi = 2/3$	$\varphi = 1/2$	$\varphi = 2/3$		
31	1.60	0.819	0.685	1.96	2.34	$0.290 \times 10^3$	$1.27 \times 10^{-3}$
37	1.43	0.935	0.783	1.53	1.92	$0.334 \times 10^3$	$1.03 \times 10^{-3}$
40	1.94	0.770	0.645	1.23	1.42	$0.344 \times 10^3$	$1.00 \times 10^{-3}$
41	1.16	0.935	0.783	<u>1.24</u>	<u>1.48</u>	$0.340 \times 10^3$	<u><math>0.82 \times 10^{-3}</math></u>
			Av.	1.49	1.79		$1.03 \times 10^{-3}$

# FIN AND TUBE RADIATOR



CS-25616

Figure 1. - Fin-and-tube radiator.

TABLE 2 DETAILS OF PHASE I FIRINGS

Target no.	Liner material	Liner I.D., in.	Liner thickness, in.	Armor material	Armor I.D., in.	Armor thickness, in.	Target temperature, °F	Target hardness at R.T. (BHN)	Projectile diameter, in.	Projectile mass, g	Projectile velocity, fps	Impact angle, deg	Crater diameter, in.	Crater depth, in.	I.D. below dimple, in.	Dimple height, in.	P/ta	Young's modulus, Yt, psi	Damage code	P corrected to 25,000 fps, P*, in.	
1	HS-25	0.460	0.020	A1	0.500	0.400	400	36	3/32	0.0160	25,500	5	0.45	0.52	0.299	0.34	0.12	0.747	9.4x10 <sup>6</sup>		0.295
3							700	37	3/32	0.0161	25,500	66	0.35	0.42	0.168	0.46	...	0.420	6.8x10 <sup>6</sup>		0.167
5							R.T.	53	3/32	0.0161	23,790	8	0.50	0.56	0.306	0.37	0.09	0.765	6.6x10 <sup>6</sup>	1e	0.316
6							700	37	1/8	0.0413	24,050	16	0.52	0.54	PERFORATED	PERFORATED			10.9x10 <sup>6</sup>		PERFORATED
7								36	3/32	0.0160	24,600	68	0.31	0.36	0.127	0.46	...	0.318	6.8x10 <sup>6</sup>	1b	0.128
9								36	3/32	0.0160	24,600	15	0.50	0.59	0.315	0.34	0.12	0.787			0.320
10								36	1/8	0.0412	23,500	41	0.63	0.73	0.476	0.23	0.23	1.19			0.496
12								37	1/8	0.0413	22,700	0	0.64	0.78	PERFORATED	PERFORATED					PERFORATED
15							R.T.	36	3/32	0.0160	24,350	0	0.42	0.47	0.544	0.26	0.20	1.36	10.9x10 <sup>6</sup>	1c	0.544
16								51	1/8?	0.0414	24,000	10	0.33	0.50	0.315	0.33	0.13	0.786			0.323
26								36	3/32	0.0160	23,950	33	0.39	0.45	0.322	0.37	0.09	0.920			0.331
27								38			26,150	40	0.41	0.47	0.281	0.34	0.12	0.937			0.279
31							700	121			23,400	12	0.31	0.33	0.150	PERFORATED		0.750	15.8x10 <sup>6</sup>	2c	0.146
32								125			23,400	10	0.30	0.33	0.225	0.06	0.065	0.941			PERFORATED
33								134			23,550	27	0.50	0.56	1.134	...	...	0.420			0.136
37								134			23,850	...	0.50	0.56	0.290	PERFORATED		0.624	6.8x10 <sup>6</sup>	2c	0.136
38								36			24,930	...	0.30	0.31	0.135	0.39	0.05	0.413	15.8x10 <sup>6</sup>	2c	0.136
39								135			24,700	13	0.28	0.30	0.109	0.11	0.015	0.741	15.8x10 <sup>6</sup>	2c	0.110
40								135			24,700	0	0.48	0.50	0.351	...	...	0.787	8.8x10 <sup>6</sup>	2c	0.348
41								36			24,700	70	0.36	0.36	0.158	0.46	...	0.395	10.9x10 <sup>6</sup>		0.159
45	HS-25	0.460	0.020	A1	0.500	0.400	500	37			24,700	27	0.50	0.55	0.252	0.37	0.09	0.650	10.9x10 <sup>6</sup>		0.251
53							R.T.			0.0159	25,200	65	0.40	0.43	0.184	...	...	0.965	6.8x10 <sup>6</sup>		0.195
54										0.0157	23,000	65	0.31	0.37	0.396	0.35	0.11	0.865	6.8x10 <sup>6</sup>		0.394
62							700			0.0160	24,500	20	0.33	0.39	0.314	0.31	0.15	0.784	6.8x10 <sup>6</sup>		0.320
64										0.0160	24,250	26	0.30	0.31	0.306	0.37	0.09	0.765	9.4x10 <sup>6</sup>		0.306
66							400			0.0156	25,000	18	0.44	0.53	0.319	0.36	0.07	0.860	6.8x10 <sup>6</sup>	1c	0.323
69										0.0151	24,400	0	0.44	0.53	0.372	0.33	0.072	1.08			0.372
71							700			0.0177	25,100	0	0.52	0.60	0.372	0.36	0.10	0.647			0.291
75										0.0152	24,700	0	0.45	0.53	0.289	0.36	0.10	0.476			0.226
79								36		0.0148	22,600	20	0.41	0.46	0.212	0.10	0.025	0.476			0.241
83								37		0.0151	25,000	0	0.40	0.42	0.241	...	...		10.9x10 <sup>6</sup>	2a	0.241
84							R.T.	36		0.0176	24,700	0	0.42	0.42	0.253	...	...		10.9x10 <sup>6</sup>	2a	0.252

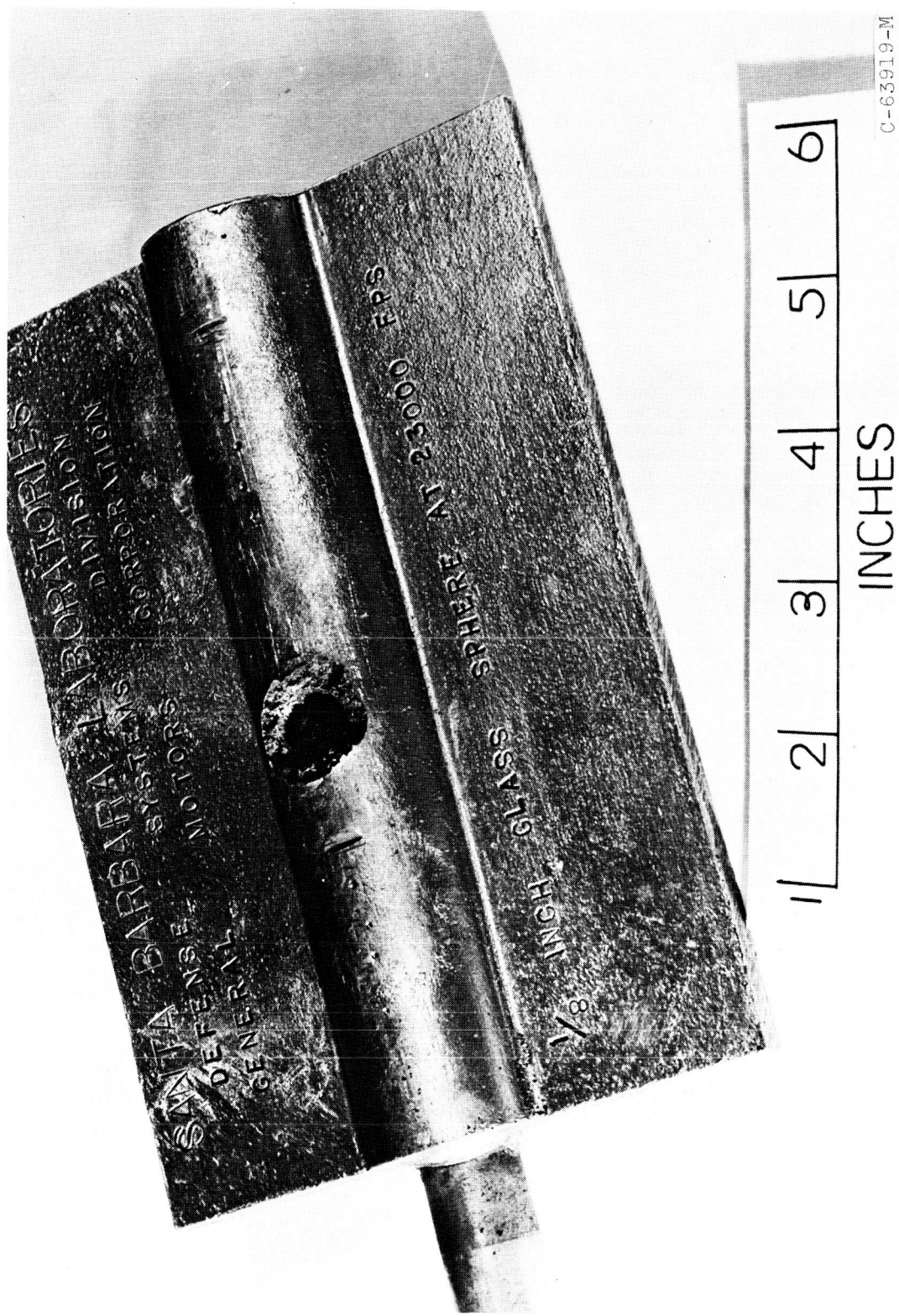


Figure 2. - Impact crater in typical radiator section, finned Al armor over HS-25 tube.

C-63919-M

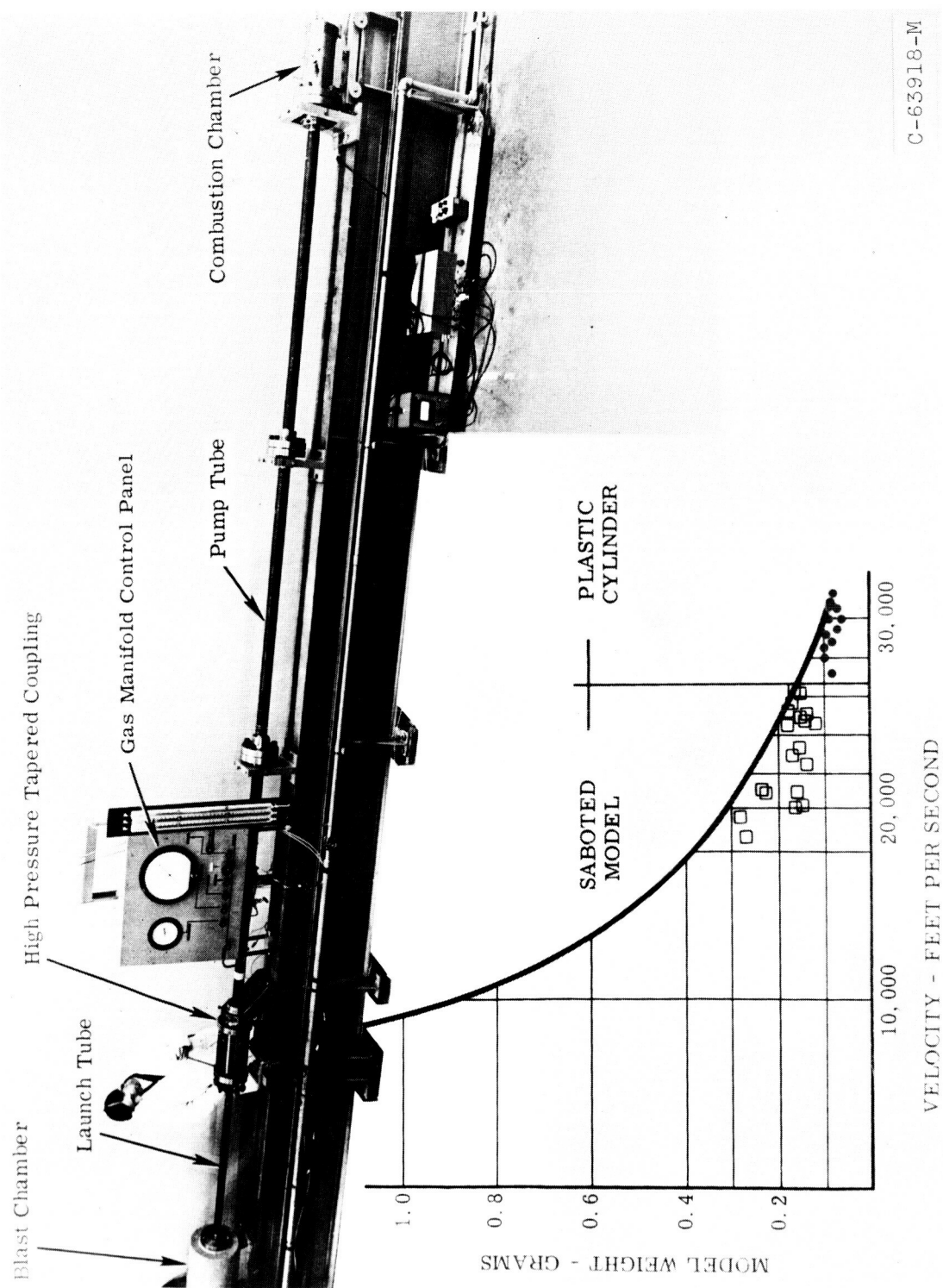


Figure 3. - 0.22 Cal. accelerated-reservoir light-gas gun.





Figure 4. - Velocity and impact chambers.

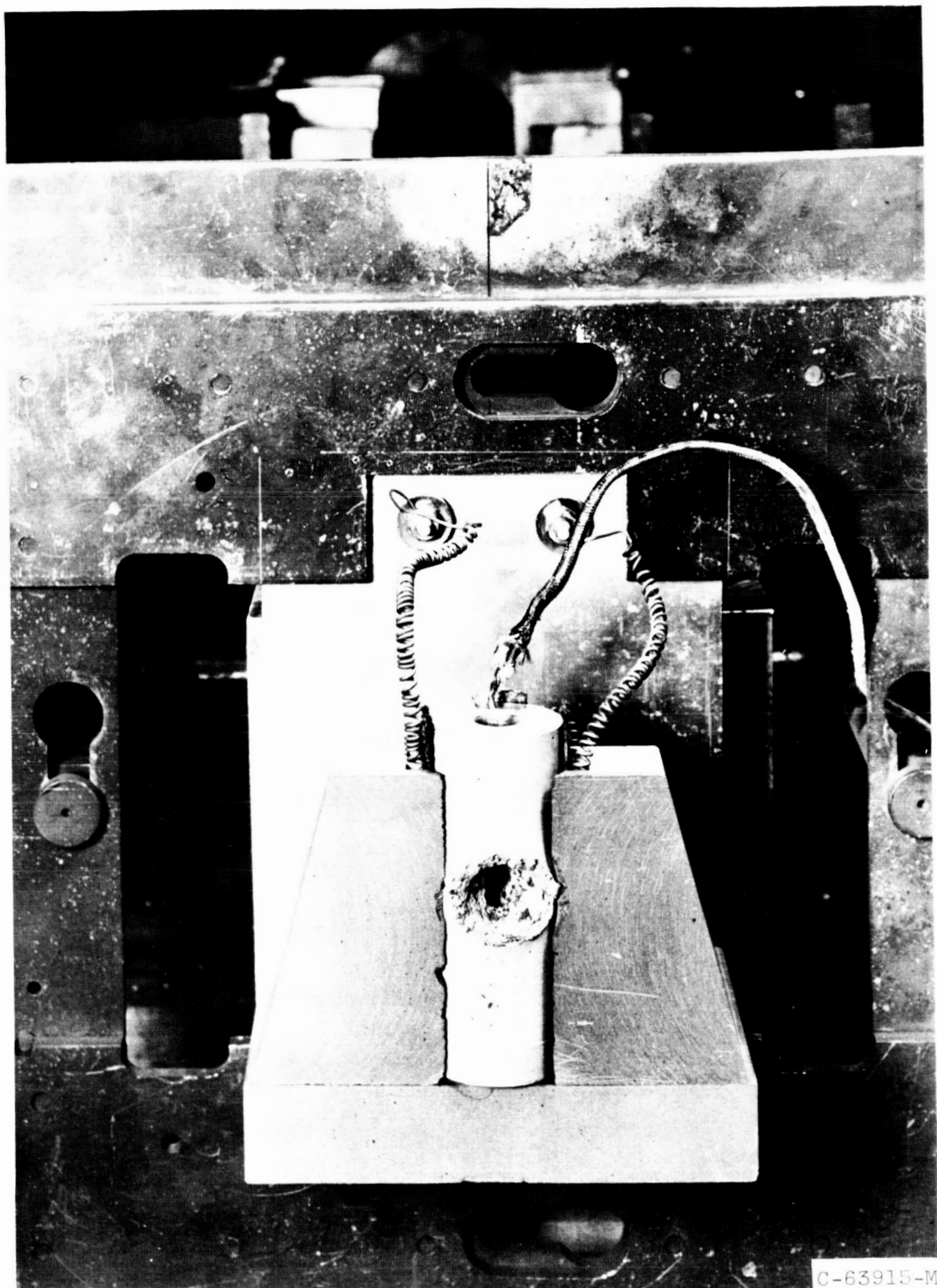
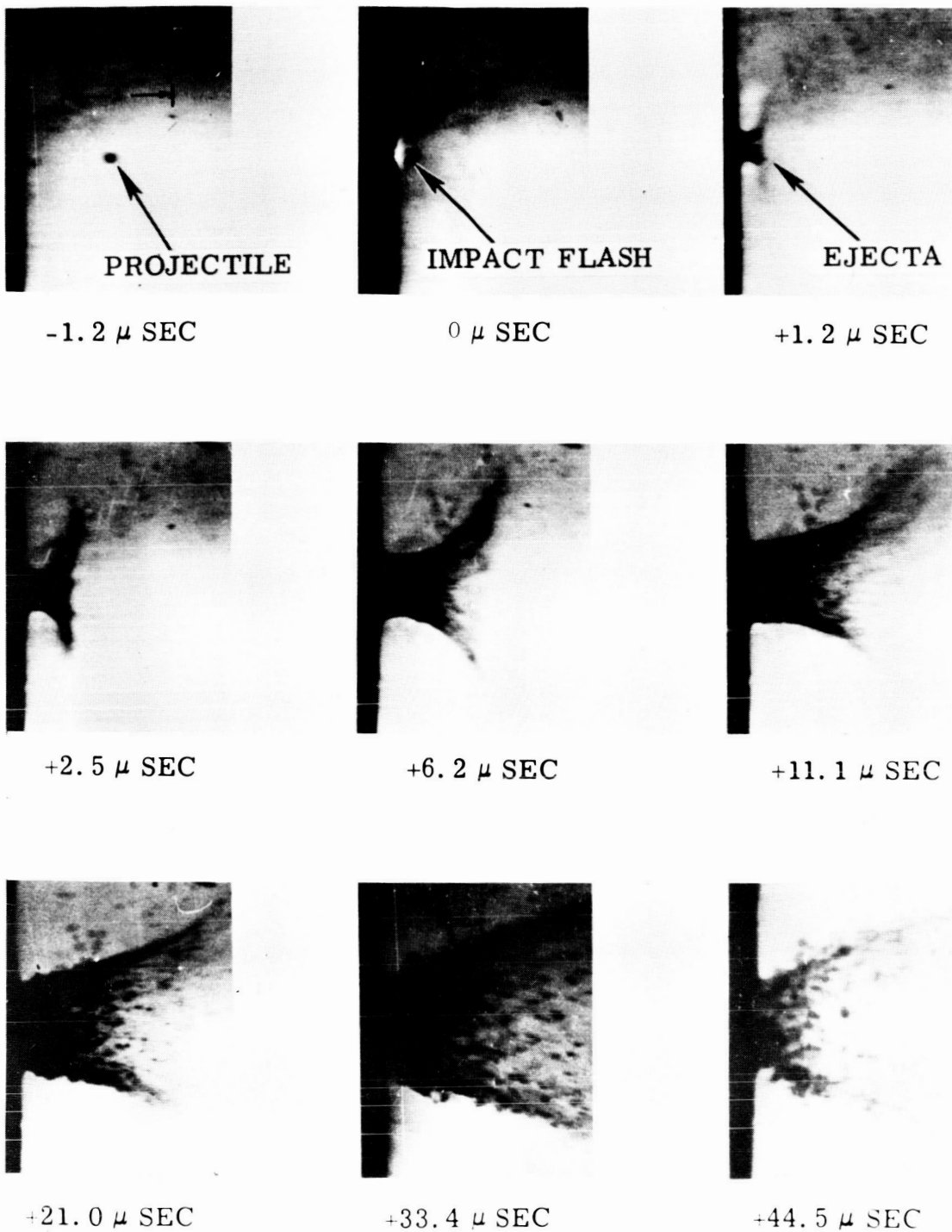
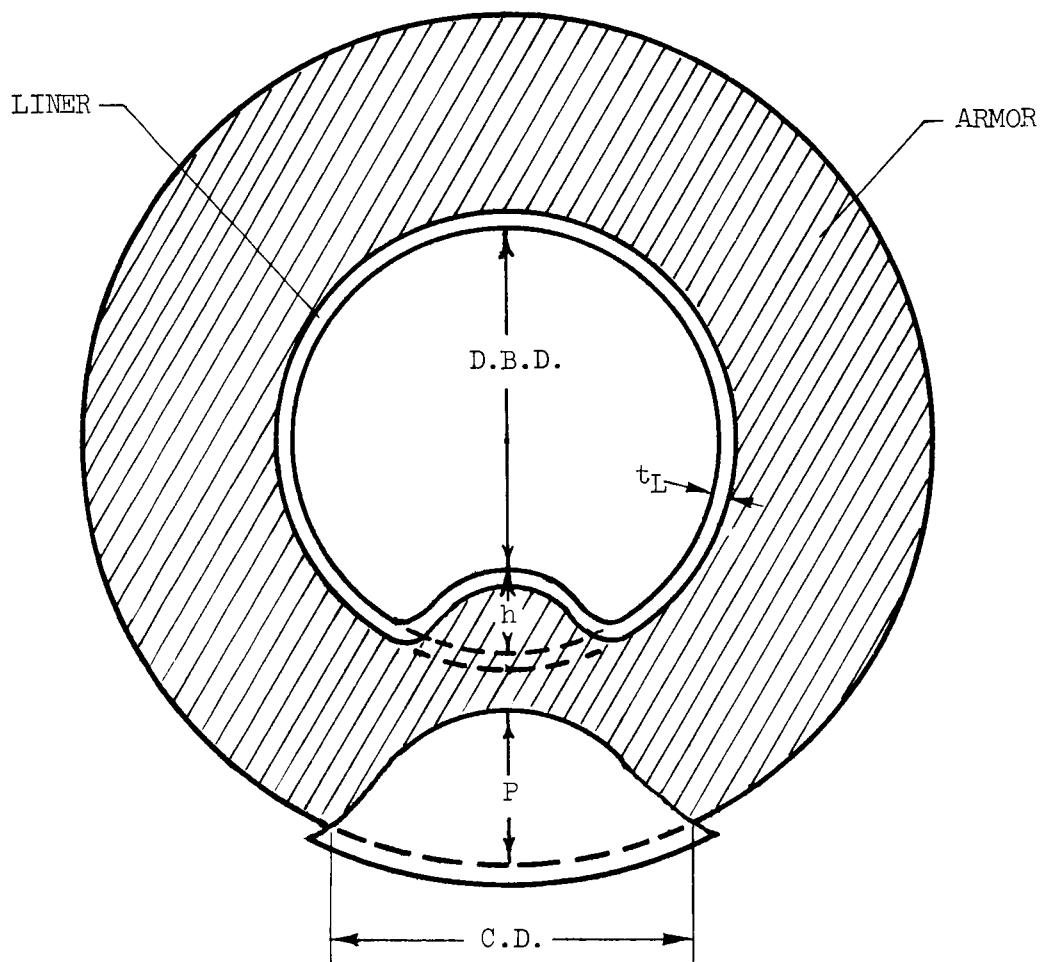


Figure 5. - Target holder, with heater elements.



C-63916-M

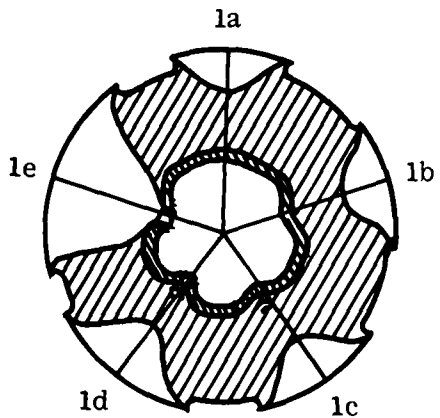
Figure 6. - B & W sequence of a 1/8" glass sphere impacting a space radiator segment at 23,000 ft/sec.



D.B.D. - I.D. BELOW DIMPLE  
 h - HEIGHT OF DIMPLE  
 P - CRATER DEPTH  
 C.D. - CRATER DIAMETER  
 $t_L$  - LINER THICKNESS

Figure 7. - Notation for target damage measurements.

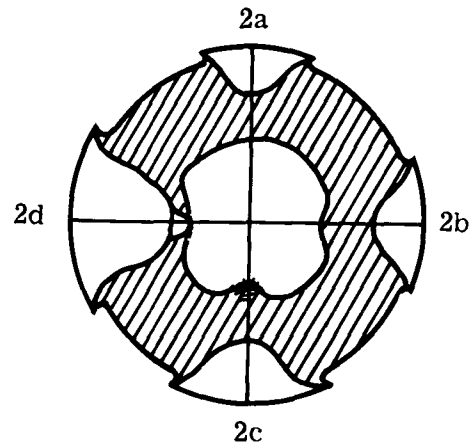
E-2161



- TYPE 1 - WITH LINER
- 1a - C, N/D, N/S, N/P
  - 1b - C, W/D, N/S, N/P
  - 1c - C, W/D, A/S, N/P
  - 1d - C, W/D, I/S, N/P
  - 1e - C, W/P

TYPE 2 - WITHOUT LINER

- 2a - C, N/D, N/S, N/P
- 2b - C, W/D, N/S, N/P
- 2c - C, W/D, I/S, N/P
- 2d - C, W/P

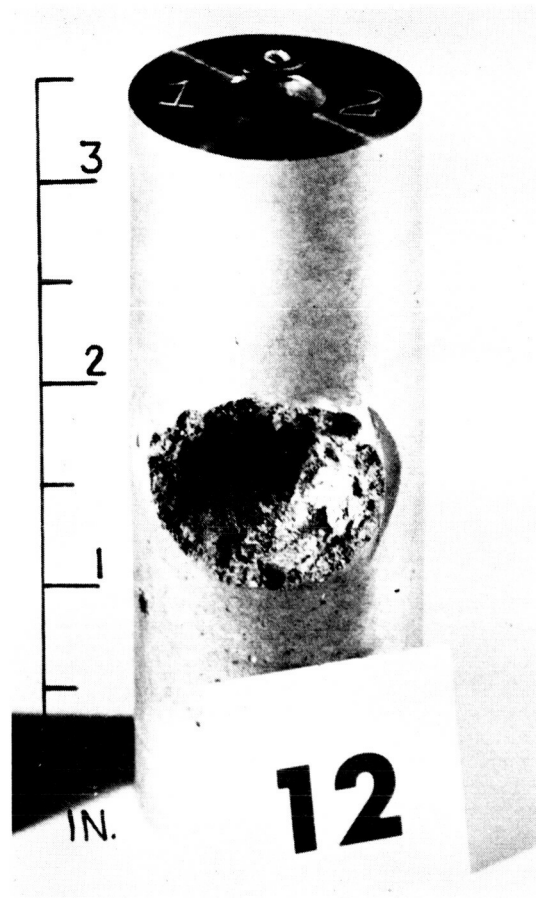
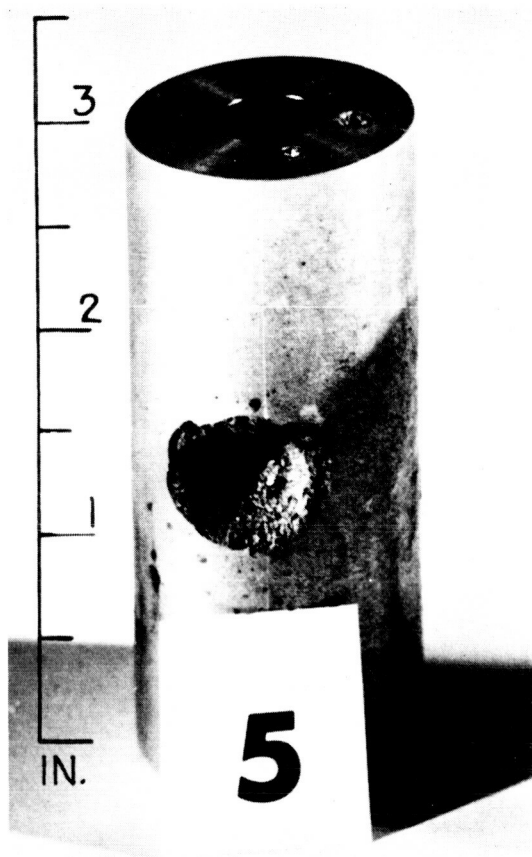


- I. D. - Inside Diameter (inches)
- O. D. - Outside Diameter (inches)
- $t_L$  - Liner Thickness (inches)
- $t_A$  - Armor Thickness (inches)
- BHN - Brinell Hardness Number
- R. T. - Room Temperature
- TAD - Target Axis Displaced (degrees)
- TAR - Target Axis Rotated (degrees)
- $\infty$  - Flat Plate

- DAMAGE CODE NUMBER -
- C - Crater
  - N/D - No Dimple
  - W/D - With Dimple
  - N/S - No Spall
  - I/S - Inner surface Spall
  - A/S - Armor internal Spall
  - N/P - No perforation
  - W/P - With Perforation

C-63913-M

Figure 8. - Damage evaluation code for sectioned targets.



3/32" GLASS SPHERE  
NO PERFORATION  
PENETRATION = 0.31"

LINER DIMPLED

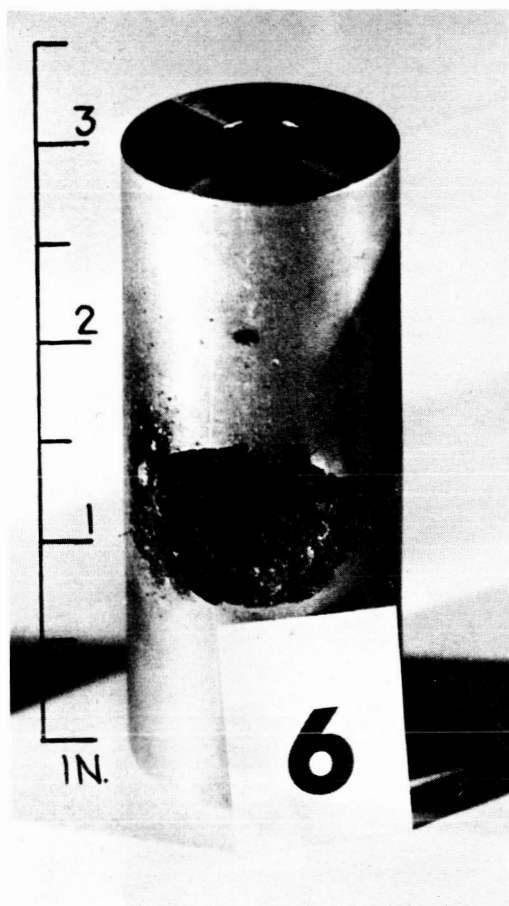
$\bar{V} = 23,250 \text{ ft/sec}$

$\bar{T} = 715^{\circ}\text{F}$

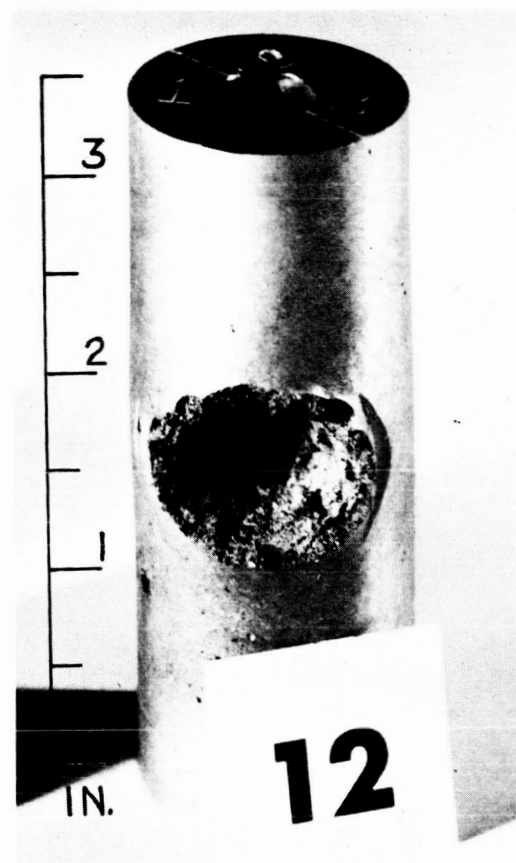
1/8" GLASS SPHERE  
PERFORATED

C-63912-M

Figure 9. - Projectile size effects, aluminum with HS-25 liner targets. Armor thickness - .400, liner thickness - .020.



ROOM TEMPERATURE  
BHN=53  
PERFORATED



700°F  
BHN=20  
PERFORATED

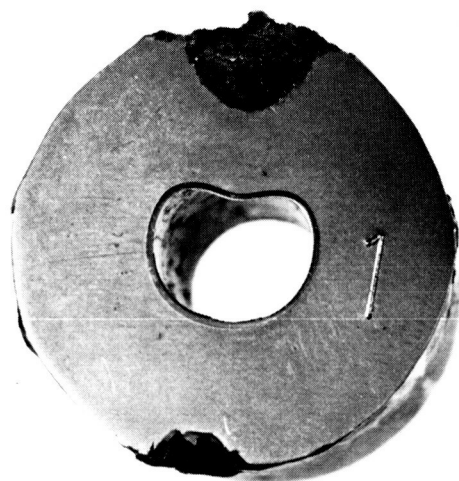
1/8" GLASS SPHERE

$\bar{V} = 23,300 \text{ ft/sec}$

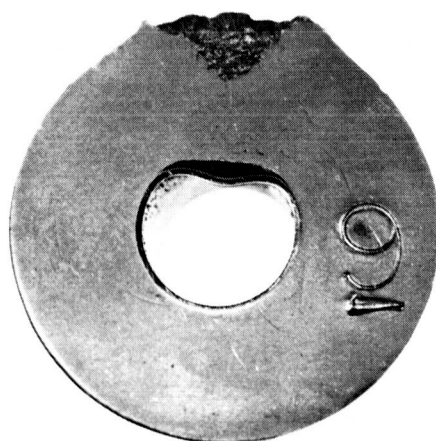
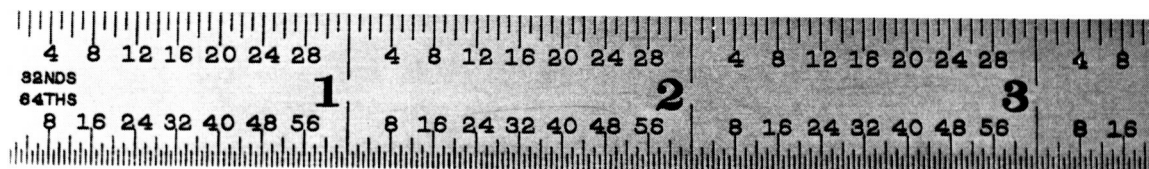
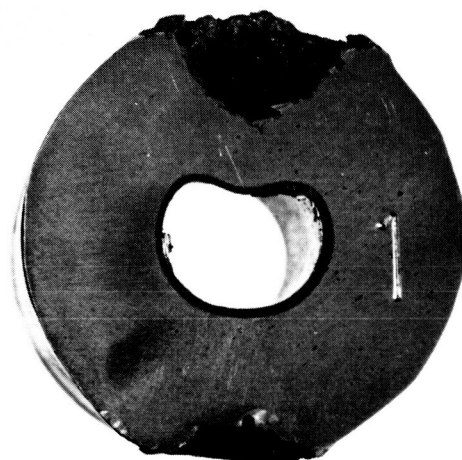
C-63917-M

Figure 10. - Target temperature effects, R.T. and 700° F. .400 aluminum armor with .020 liner targets.





T = 400°F  
BHN = 25



T = 700°F  
BHN = 20

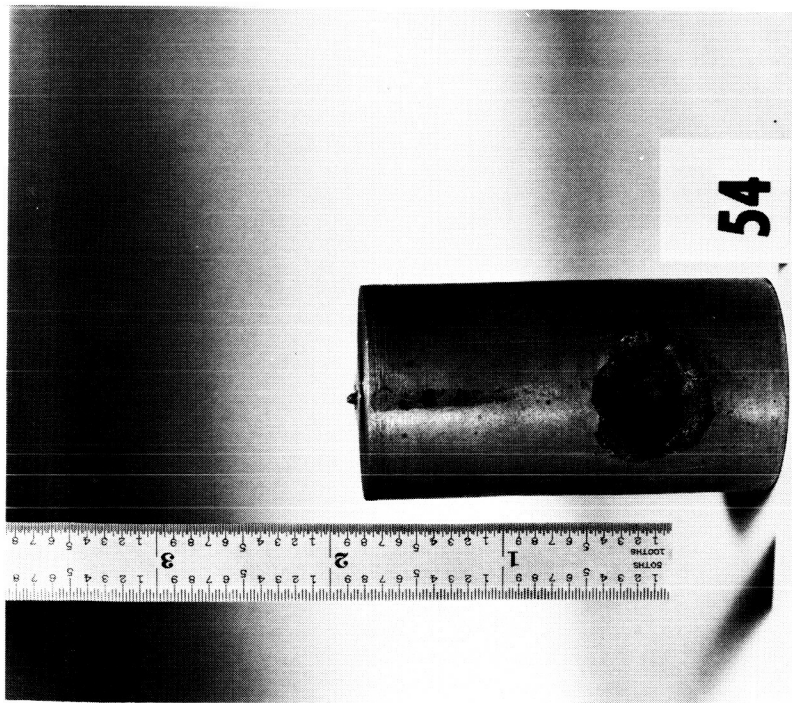


C-63841-M

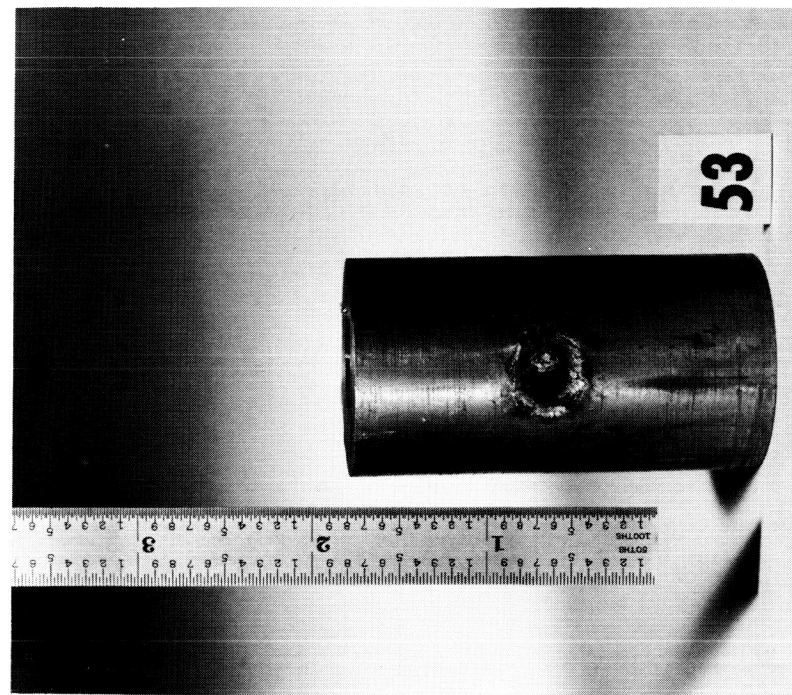
SECTION VIEW OF CRATER AT MAXIMUM DEPTH

Figure 11. - Target temperature effects, 400 and 700° F. .400 aluminum armor with .020 liner targets. 3/32" glass projectile at 24,600 ft/sec.





IMPACT ANGLE - 27°  
CRATER DEPTH - .252"



3/32" GLASS SPHERE

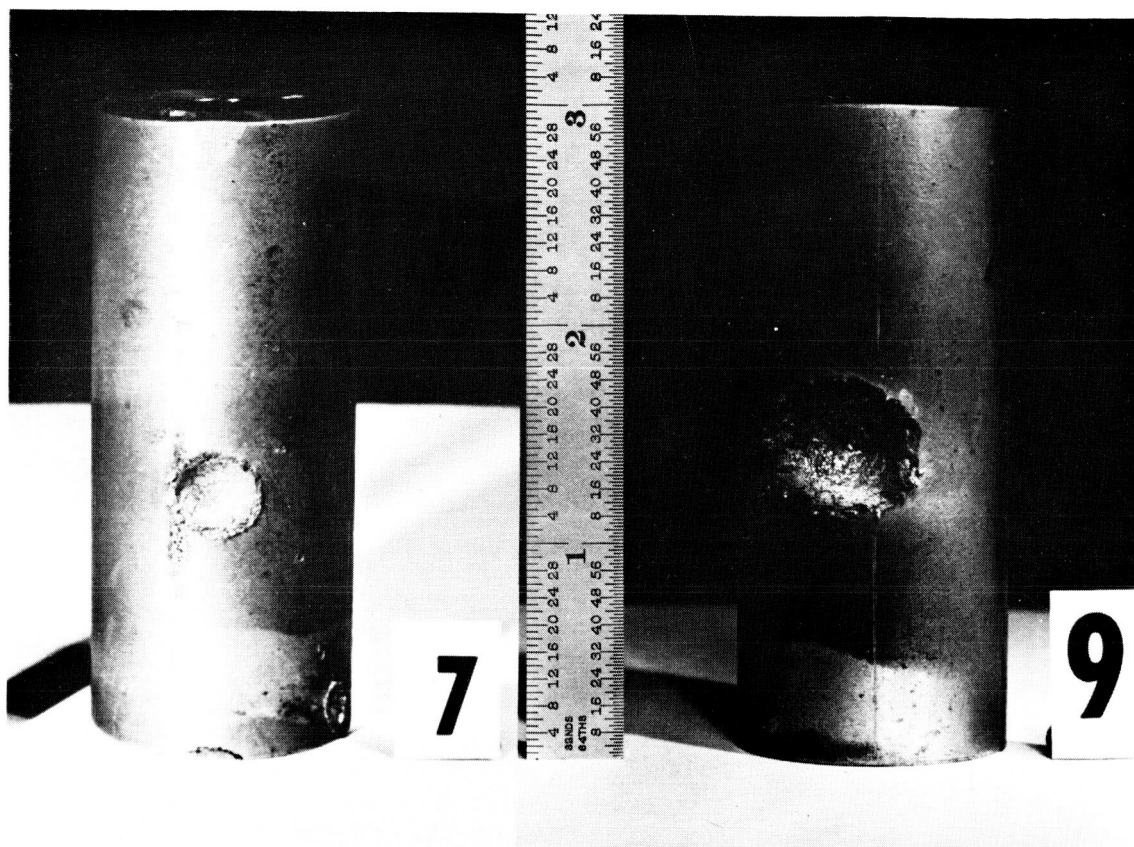
$\bar{V} = 24,900$  ft/sec.

ROOM TEMP.

IMPACT ANGLE - 70°  
CRATER DEPTH - .158"

C-64100

Figure 12. - Impact angle effects, .500 I.D. aluminum, .400" thick, HS-25 liner.



68° FROM CENTER  
NO PERFORATION  
PENETRATION; 0.13"

15° FROM CENTER  
NO PERFORATION  
PENETRATION; 0.34"

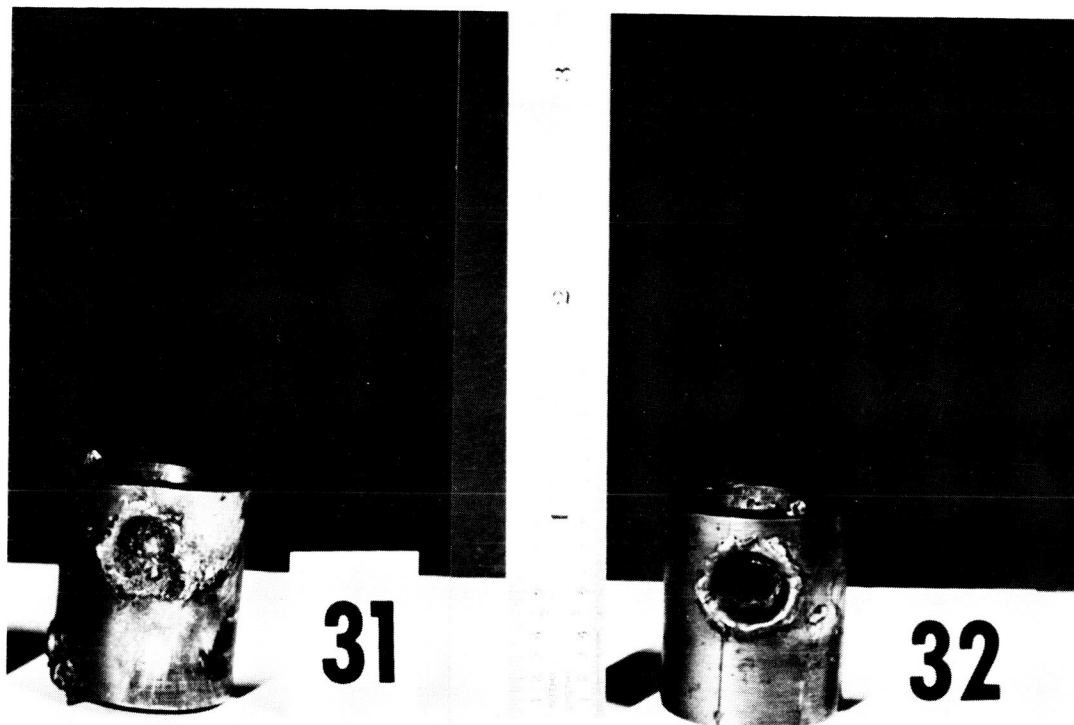
3/32" GLASS SPHERE

$\bar{v} = 24,450 \text{ ft/sec}$

$\bar{T} = 700^{\circ}\text{F}$

C-64409

Figure 13. - Impact angle effects, .500" I.D. aluminum .400" thick, with HS-25 liner.



40° FROM CENTER  
NO PERFORATION  
PENETRATION; .150"

12° FROM CENTER  
PERFORATED

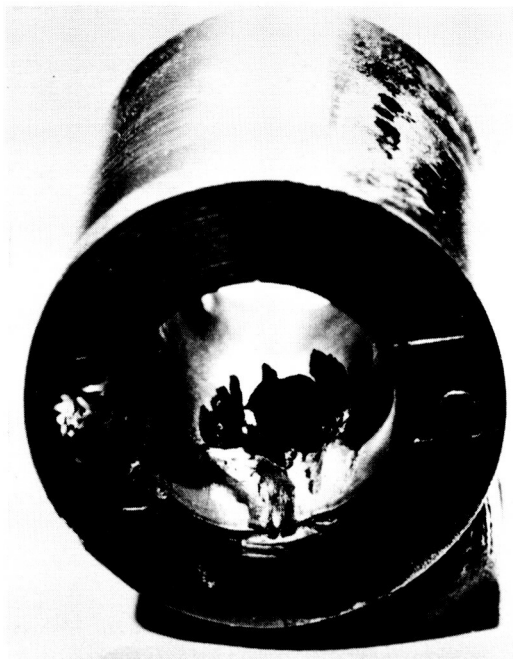
3/32" GLASS SPHERE

$\bar{V} = 25,650$  ft/sec

$\bar{T} = 700^{\circ}\text{F}$

C-64104

Figure 14. - Impact angle effects, .460 I.D. columbium .200" thick, no liner.



ALL COLUMBIUM 0.20" THICK WALL    0.40" AL. ARMOR, 0.02" HS-25 LINER  
 NO PERFORATION - INTERNAL SPALL    NO PERFORATION - INTERNAL DIMPLING  
 3/32" GLASS SPHERE    1/8" GLASS SPHERE

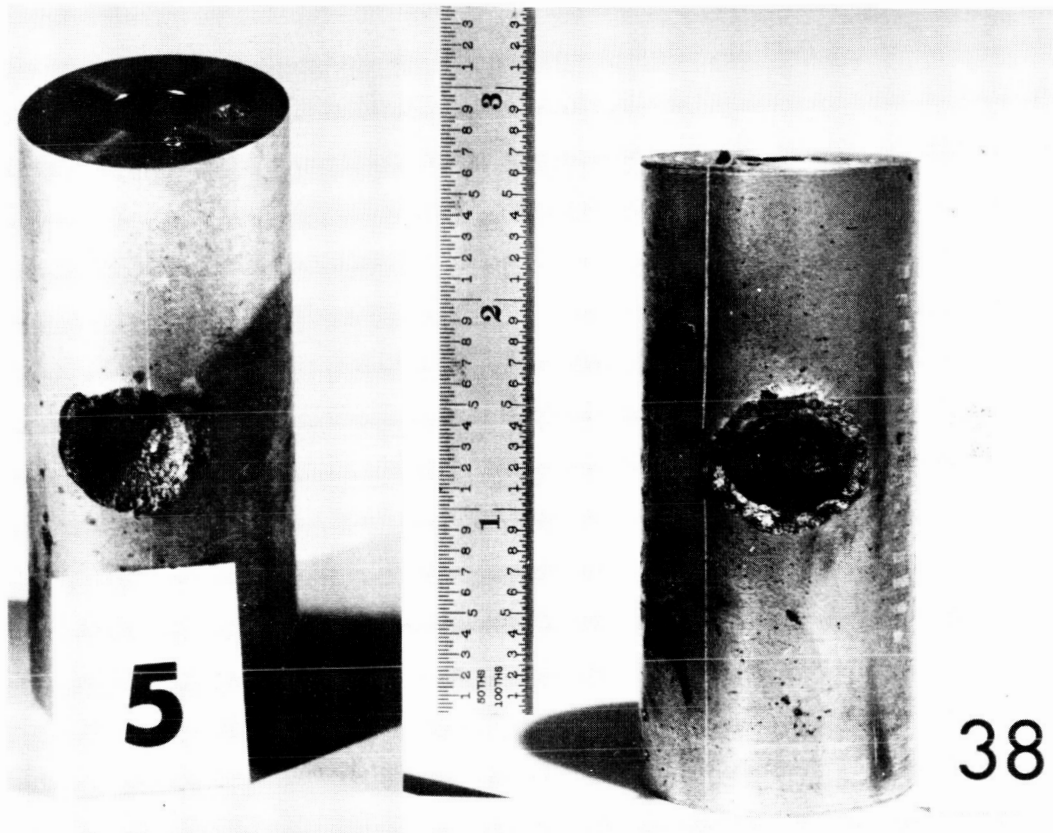
TUBE I.D. = .460"

$\bar{V} = 24,700$  ft/sec

$\bar{T} = 700^{\circ}\text{F}$

C-64106

Figure 15. - Internal tube damage. Equal weight per unit length of tube.



0.40" Al. ARMOR 0.02" HS-25 LINER  
 NO SPALL ON INSIDE  
 NO PERFORATION  
 DIMPLE

0.47" Al. ARMOR, NO LINER  
 SPALL ON INSIDE  
 NO PERFORATION

3/32" GLASS SPHERE

$\bar{V} = 24,650$  ft/sec

$\bar{T} = 715^{\circ}\text{F}$

C-64109

Figure 16. - Liner effects, aluminum targets. Equal weight per unit length of tube.

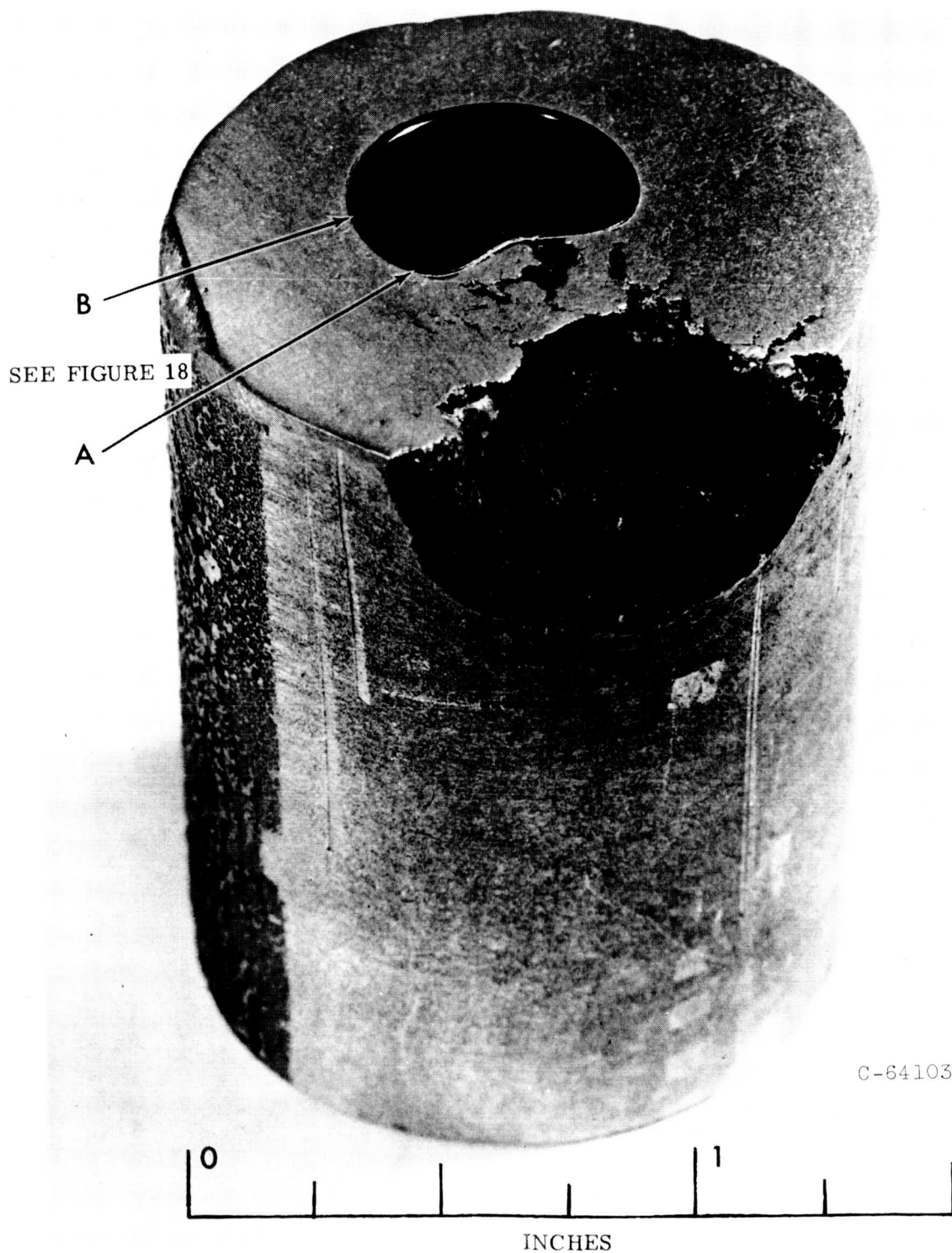
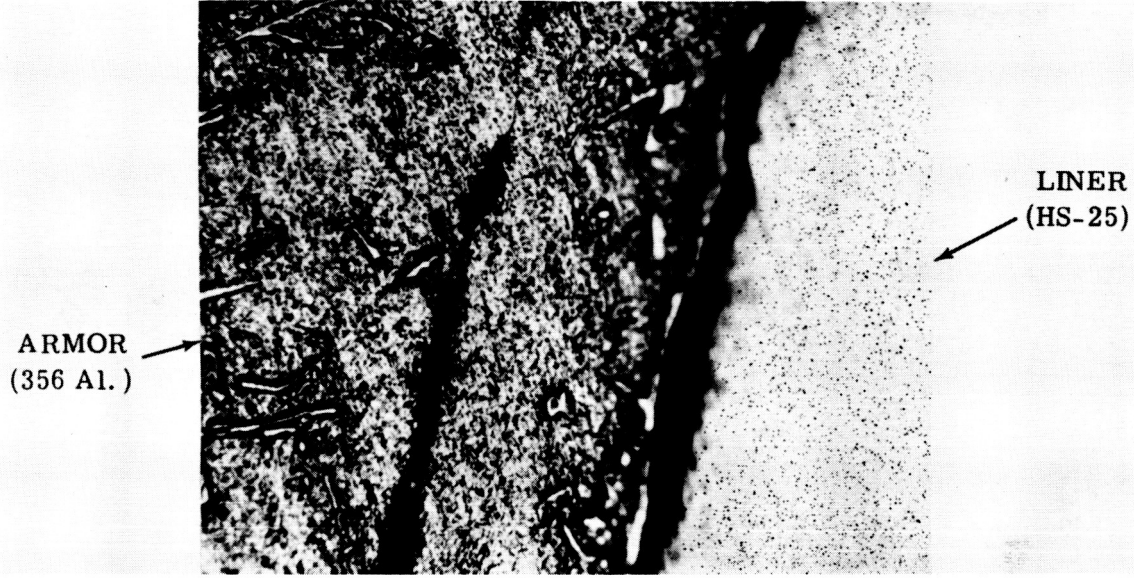


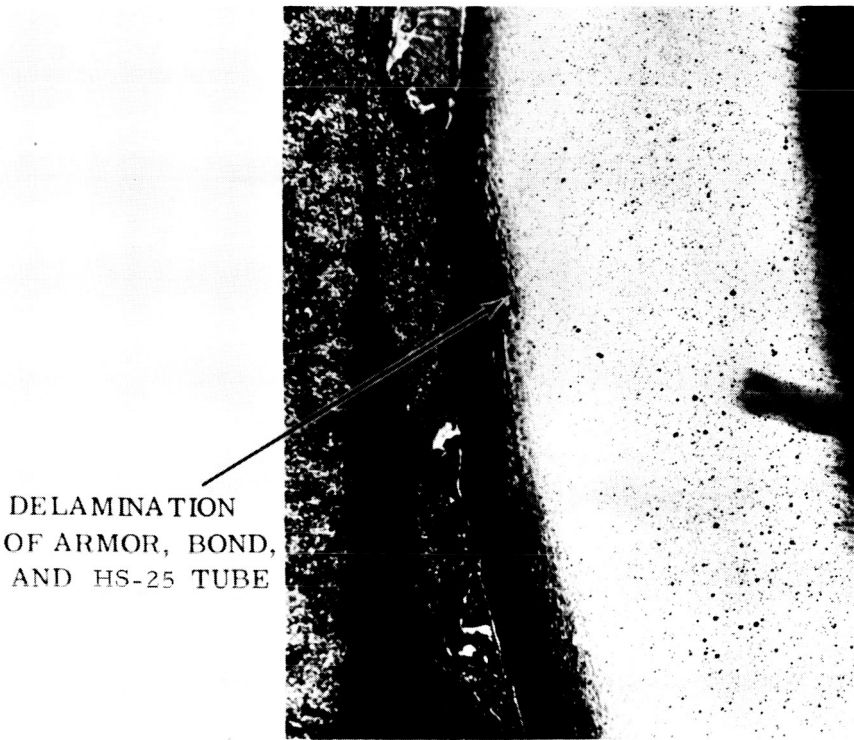
Figure 17. - Typical impact crater section, aluminum with HS-25 liner target.



E-2161



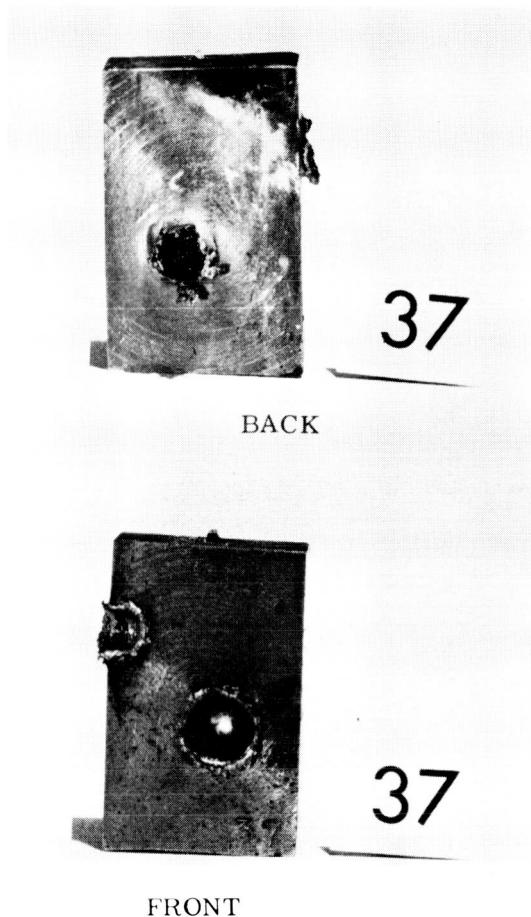
SECTION B (300X)



C-64108

SECTION A (120X)

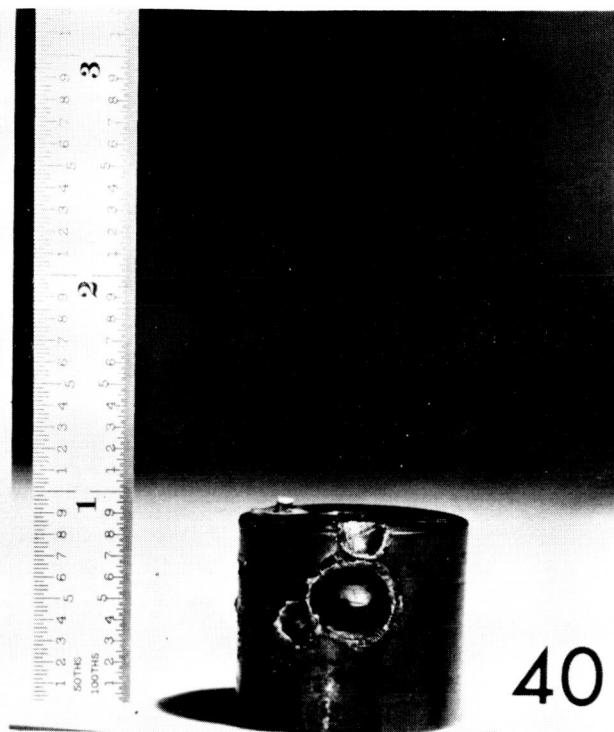
Figure 18. - Armor-liner interface photomicrographs-  
reference Fig. 15.



BACK

FRONT

0.320" THICK PLATE  
NO PERFORATION  
BACK SPALL



0.320" THICK WALL, .460 I.D.  
NO SPALL ON INSIDE  
NO PERFORATION

3/32" GLASS SPHERE

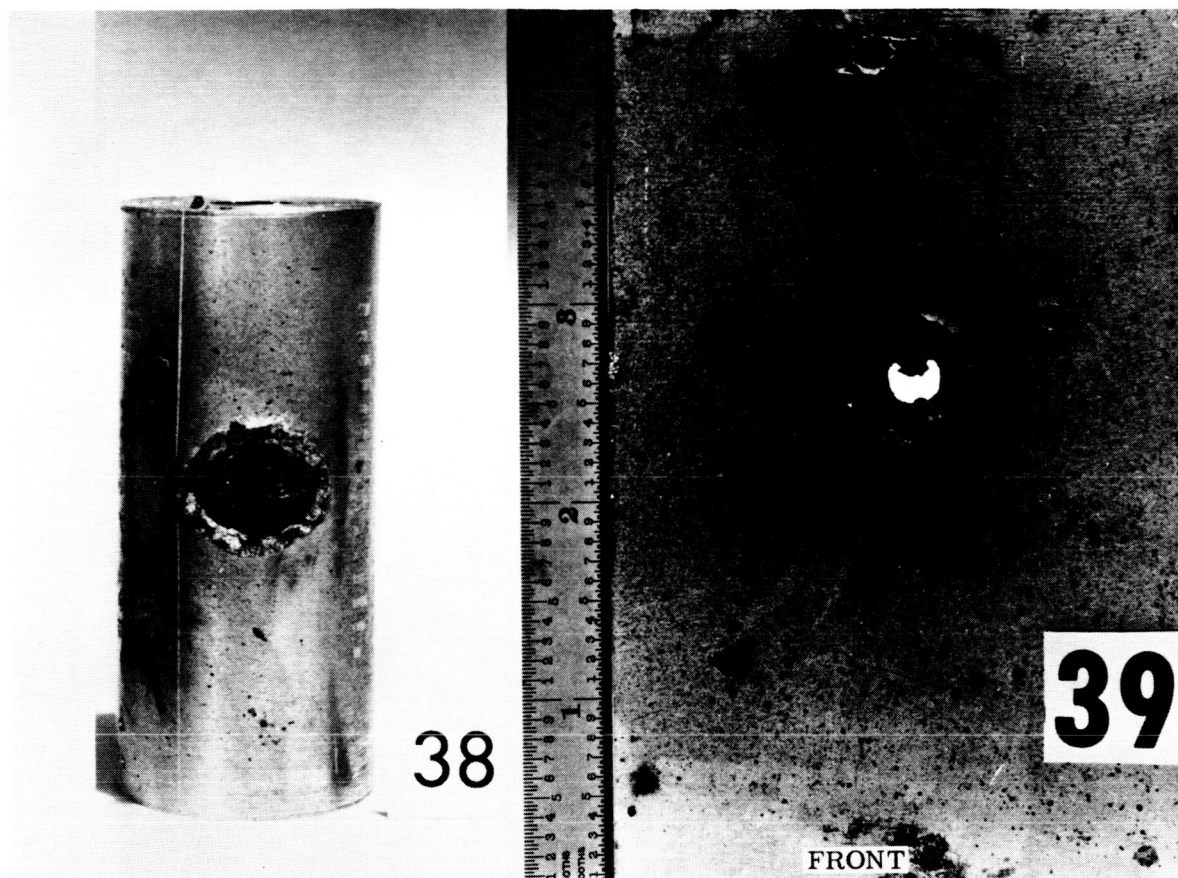
$\bar{V} = 24,500$  ft/sec.

$\bar{T} = 700^{\circ}\text{F}$

C-64101

Figure 19. - Target radius effects, Cb targets.





0.465" THICK WALL, .420" I.D.  
NO PERFORATION

0.446" THICK PLATE  
PERFORATED

3/32" GLASS SPHERE

$\bar{V} = 25,000$  ft/sec

$\bar{T} = 700^{\circ}\text{F}$

C-64111

Figure 20. - Target radius effects, aluminum targets - no liner.



45

83



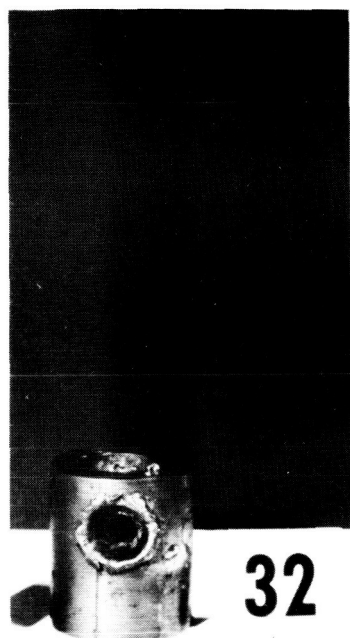
2.5" I.D.  
PENETRATION - .315"  
INTERNAL SPALL

.125" I.D.  
PENETRATION - .212"  
NO SPALL

$\bar{V} = 24,000$  FT/SEC.  
 $\bar{T} = 600^\circ\text{F}$

C-64107

Figure 21. - Tube radius effects. Aluminum armor, .446" thick. No liner.



.460" I.D, .200" THICK WALL  
ALL COLUMBIUM  
PERFORATED



.500" I.D, .400" THICK WALL  
AL. ARMOR. HS-25 LINER  
PENETRATION; .315"

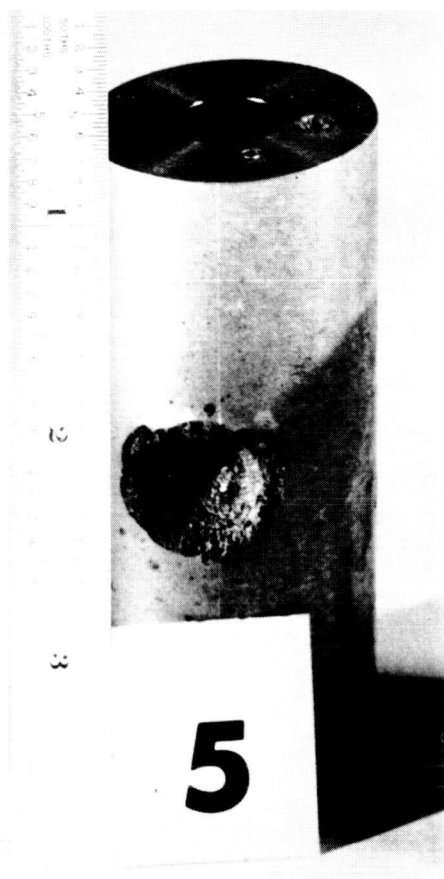
3/32" GLASS SPHERE

$\bar{V} = 24,800$  ft/sec

$\bar{T} = 700^{\circ}\text{F}$

C-64102

Figure 22. - Comparison of equal unit weight aluminum and columbium targets.



0.40" AL-0.02" HS25 LINER  
PENETRATION; .306"



ALL COLUMBIUM, 0.320" WALL  
PENETRATION; .135"

3/32" GLASS SPHERE

$\bar{V} = 24,500 \text{ ft/sec}$

$\bar{T} = 715^{\circ} \text{ F}$

C-64105

Figure 23. - Comparison of equal protection schemes (NASA Ref. 1)  
I.D. constant.

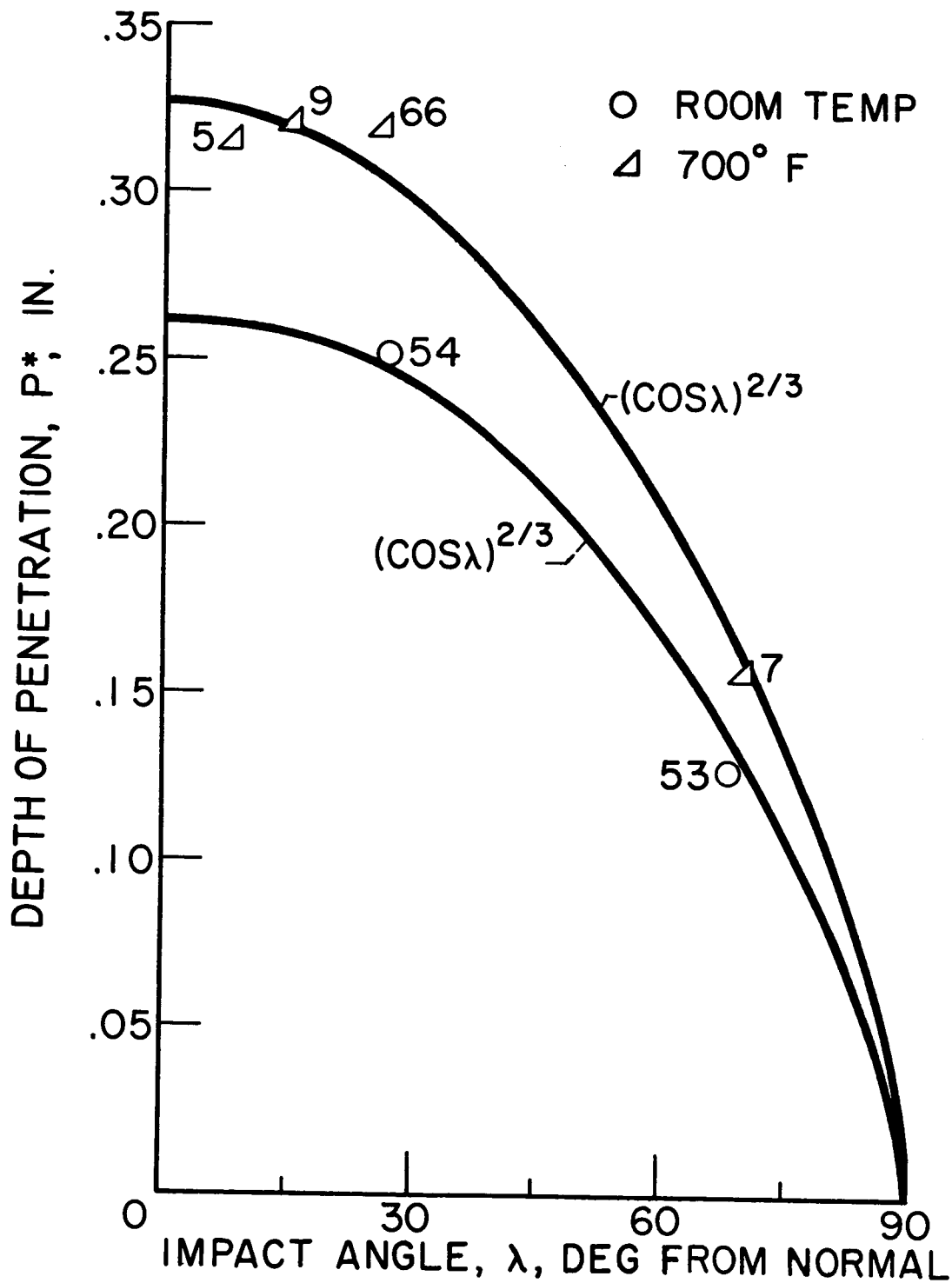


Figure 24. - Variation of penetration depth with impact angle. Cast aluminum tubes, 3/32" glass particle, 25,000 ft/sec.

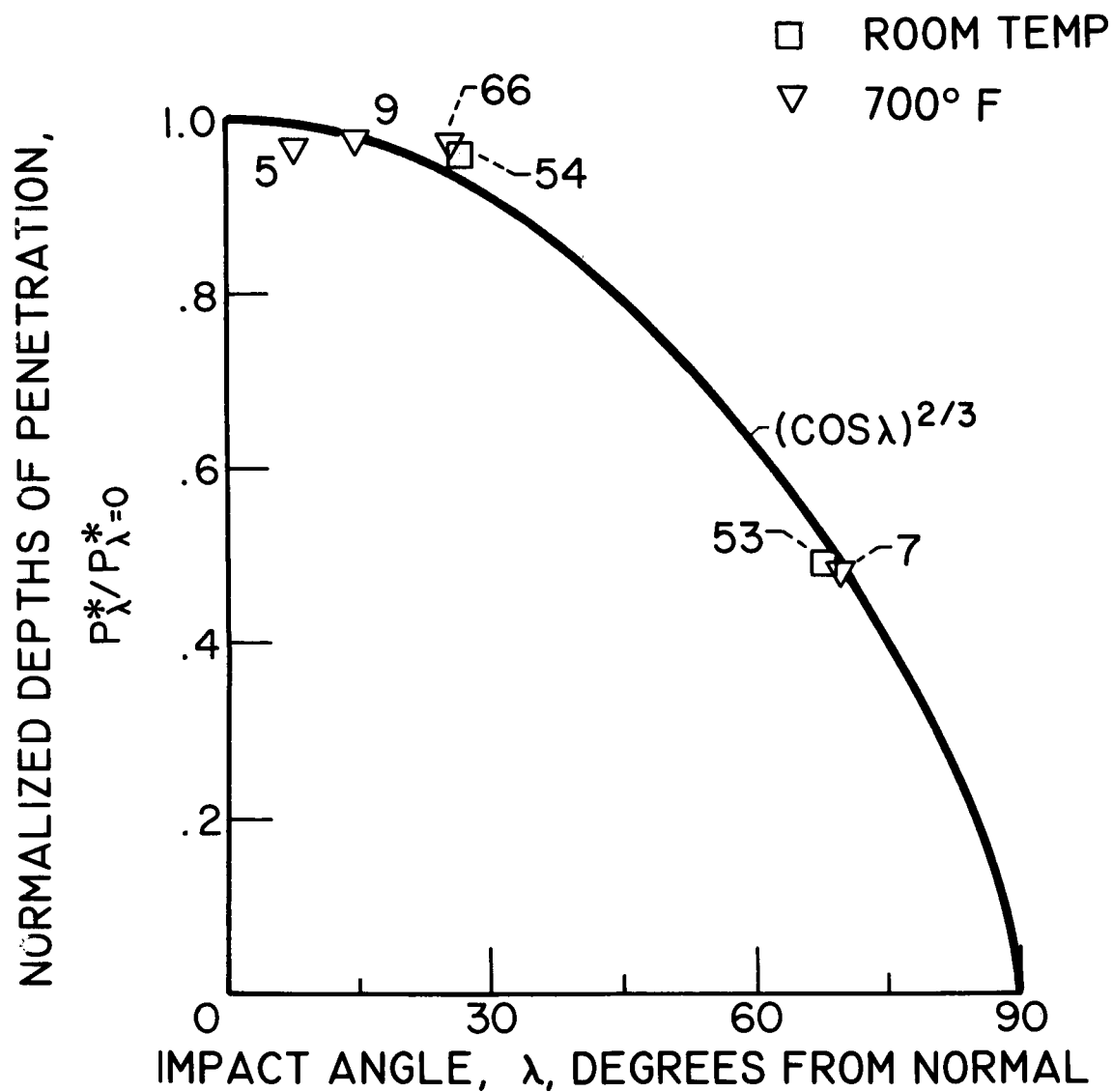


Figure 25. - Normalized variation of depth of penetration with impact angle. Cast aluminum tubes, 3/32" glass projectile, 25,000 ft/sec.

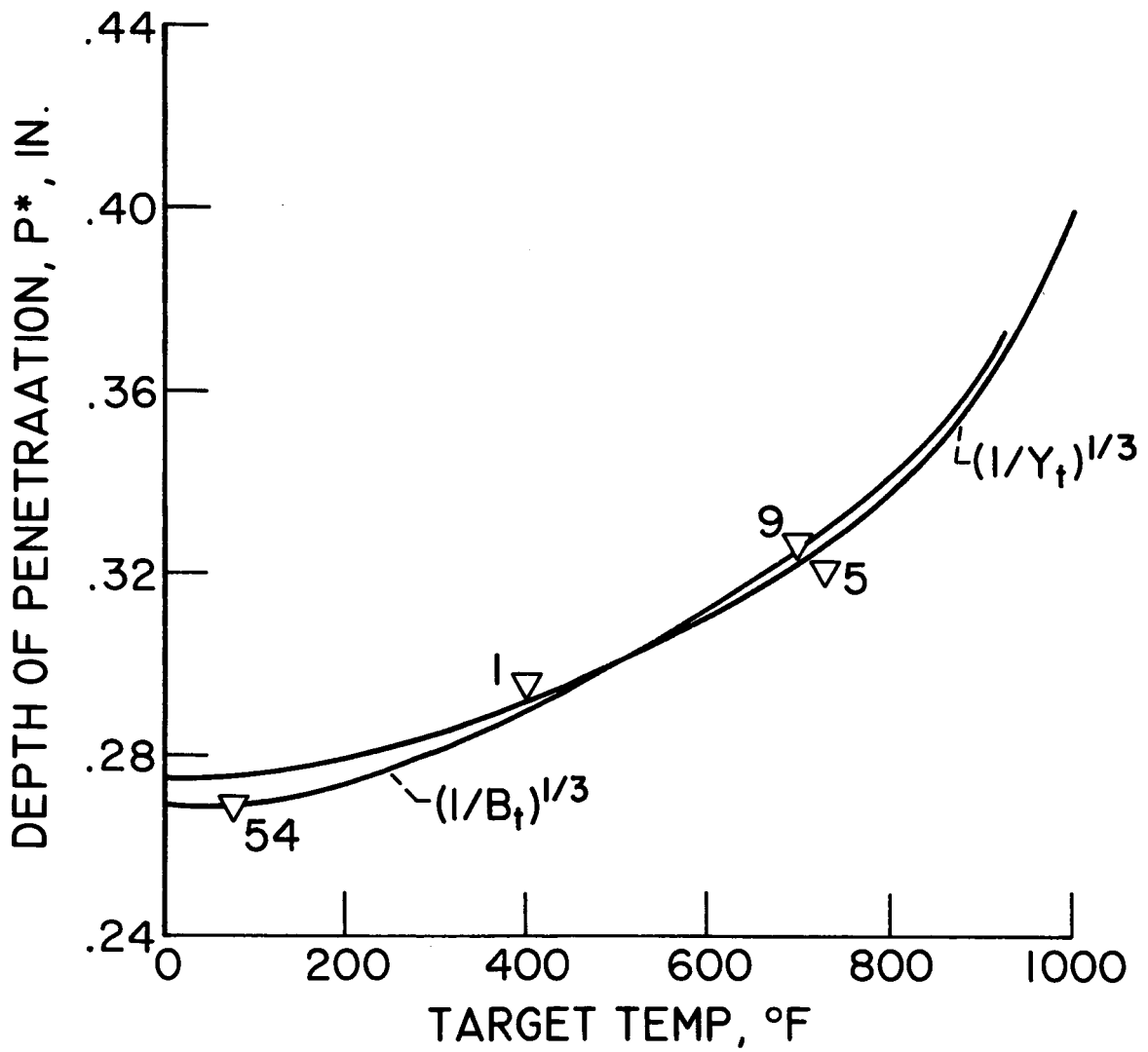


Figure 26. - Variation of depth of penetration with target temperature. Cast aluminum tubes, normal impact 3/32" diam. glass particle, 25,000 ft/sec.

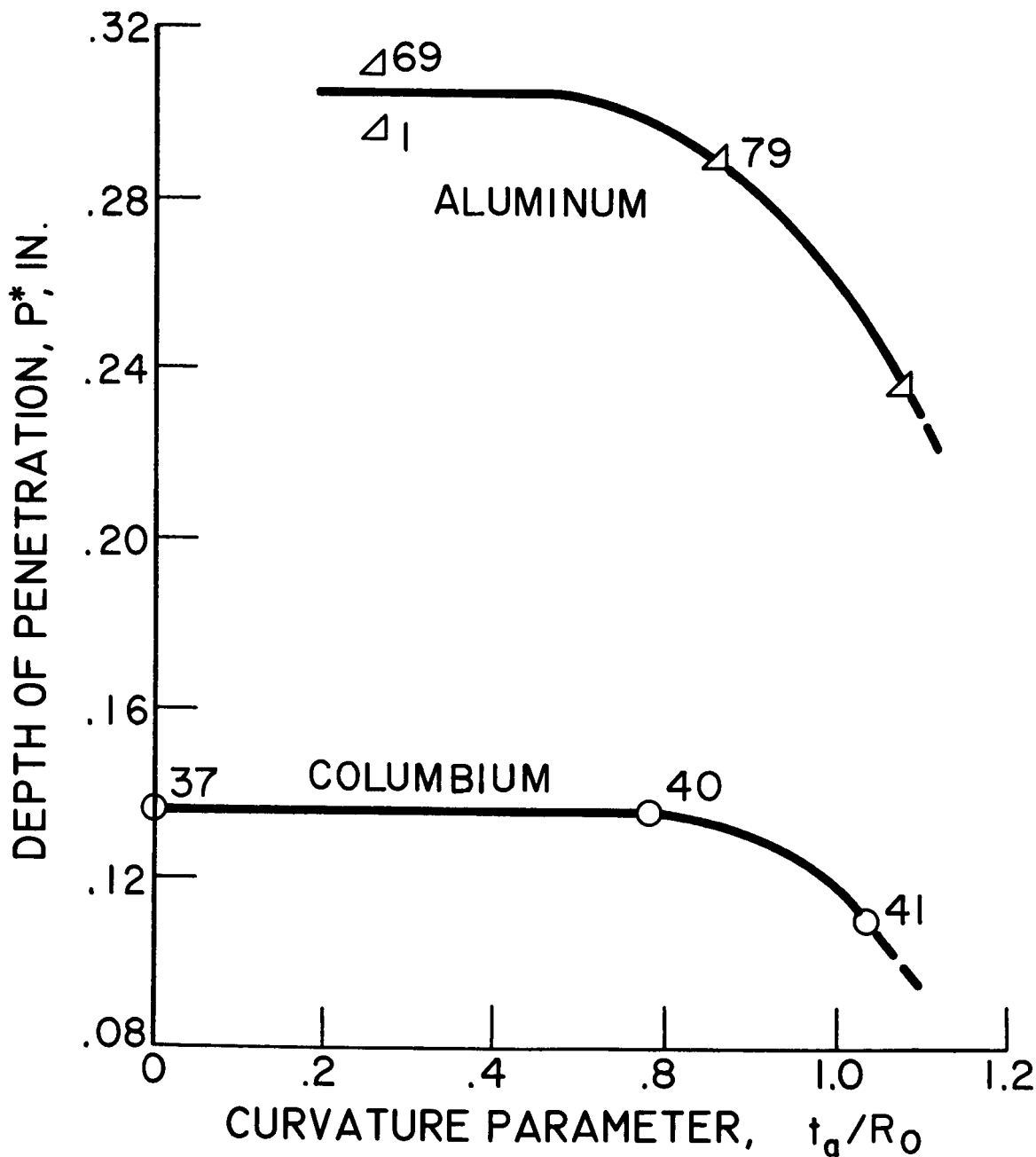


Figure 27. - Variation of depth of penetration with tube radius. 700° F, 3/32" diam. glass particle, 25,000 ft/sec.



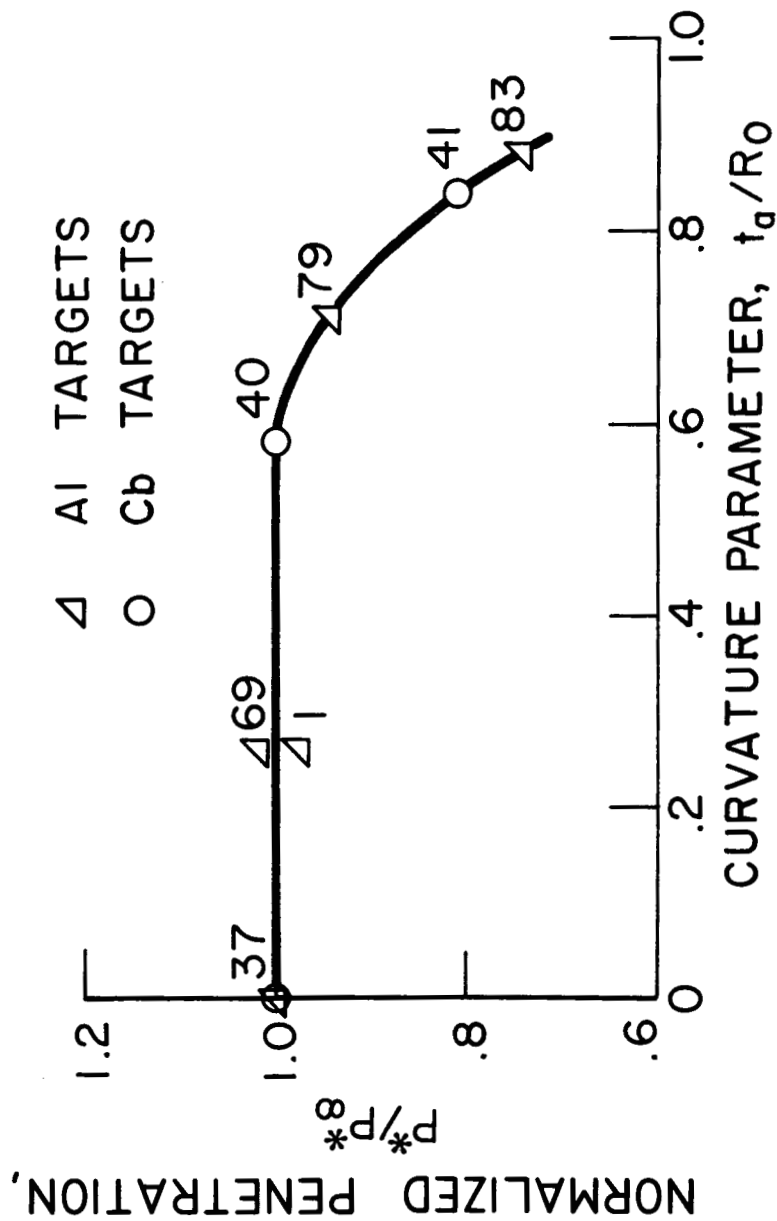


Figure 28. - Variation of normalized depth of penetration with tube radius. 700° F, 3/32" diam. glass particle, 25,000 ft/sec.

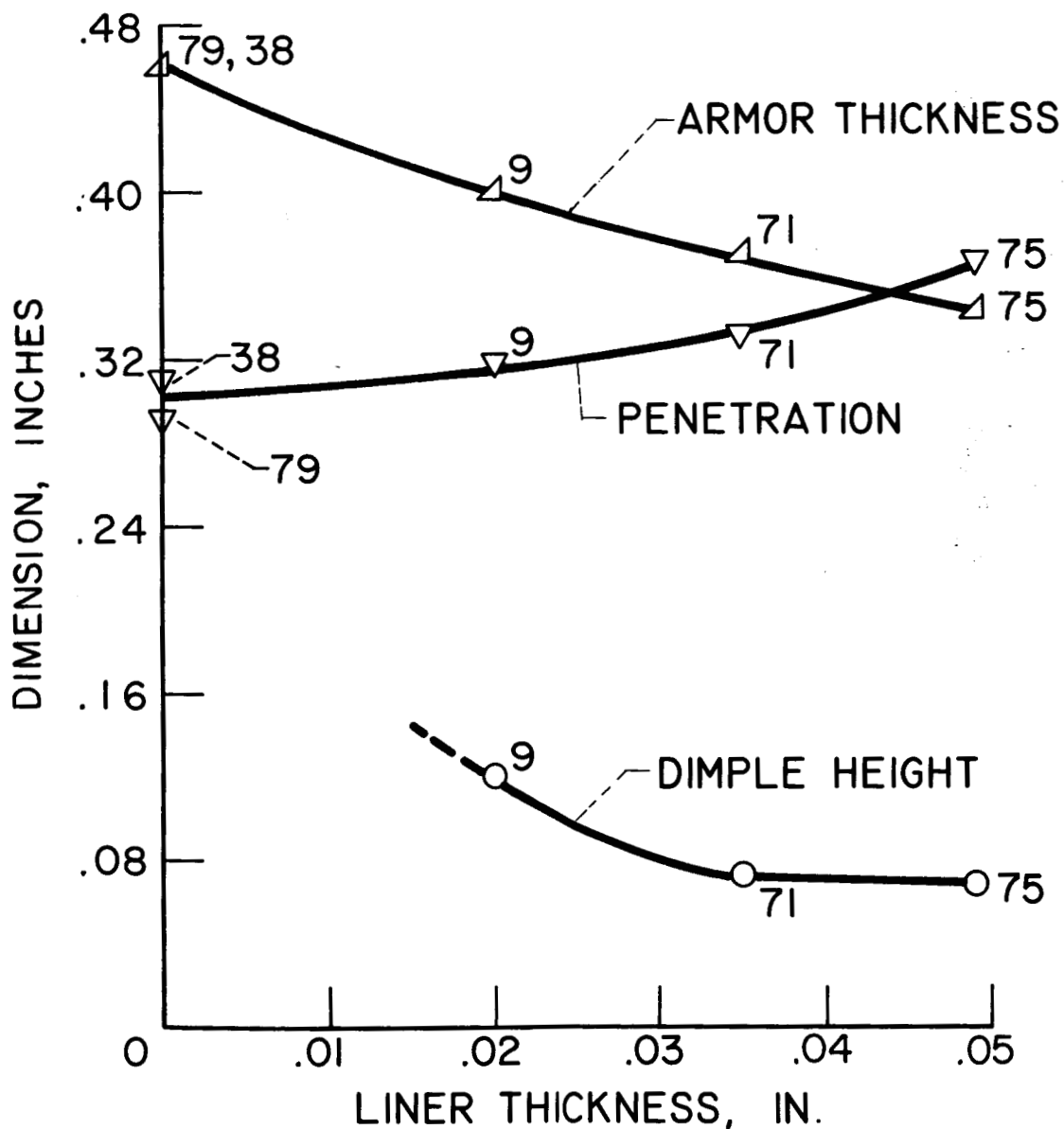


Figure 29. - Variation of depth of penetration and dimple height with liner thickness. Cast aluminum on HS-25, equal weight configurations. 3/32" diam. particle, 25,000 ft/sec, 700° F.